

# Silicate Weathering in the Semi-Arid Southern Pyrenees During the PETM: Lithium Isotope Evidence

Rocio Jaimes-Gutierrez<sup>1</sup>, Marine Prieur<sup>1</sup>, David J. Wilson<sup>2</sup>, Philip A.E. Pogge von Strandmann<sup>2,3</sup>, Emmanuelle Pucéat<sup>4</sup>, Thierry Adatte<sup>5</sup>, Jorge E. Spangenberg<sup>6</sup>, Sébastien Castellort<sup>1</sup>

<sup>1</sup> Department of Earth Sciences, University of Geneva, Rue des Maraichers 13, 1205, Geneva, Switzerland

<sup>2</sup> London Geochemistry and Isotope Centre (LOGIC), Institute of Earth and Planetary Sciences, University College London and Birkbeck, University of London, Gower Street, London WC1E 6BT, UK

<sup>3</sup> Institute of Geosciences, Johannes Gutenberg University Mainz, Mainz, Germany

<sup>4</sup> Biogéosciences Dijon, Université Bourgogne Franche – Comté, UMR CNRS 6282, Dijon, France.

<sup>5</sup> Institute of Earth Sciences, Géopolis, University of Lausanne, 1015 Lausanne, Switzerland

<sup>6</sup> Institute of Earth Surface Dynamics, Géopolis, University of Lausanne, 1015 Lausanne, Switzerland

Correspondence to: Rocio Jaimes-Gutierrez, Rocio.JaimesGutierrez@unil.ch

## Abstract

The Palaeocene-Eocene Thermal Maximum (PETM), a hyperthermal event ~56 Ma ago, allows the Earth system response to abrupt climate change to be explored. Recent investigations link the PETM with a negative lithium isotope ( $\delta^7\text{Li}$ ) excursion, interpreted as an increase in continental silicate weathering fluxes, which can regulate Earth's surface temperature over geological timescales. However, the silicate weathering response under different climatic regimes has yet to be constrained. Here we aim to address the chemical weathering response to the PETM in the semi-arid Southern Pyrenees, and to explore how different archives (i.e. clays and carbonate nodules) record the weathering changes.

We investigated two continental sections in the southern Pyrenees. In the Esplugafreda section, we measured  $\delta^7\text{Li}$  values as a silicate weathering proxy and  $\epsilon_{\text{Nd}}$  values as a provenance proxy in the clay minerals. In the Rin section, we characterised the PETM locally by analysing  $\delta^{13}\text{C}$  values in organic matter and examined the clay mineralogy in the paleosols, as well as measuring  $\delta^7\text{Li}$  values in clays and carbonate nodules to trace silicate weathering. In the Esplugafreda section, we observe temporally stable  $\epsilon_{\text{Nd}}$  values, while the  $\delta^7\text{Li}_{\text{clays}}$  record shows two small positive excursions, one during the Pre-Onset Excursion (~0.7‰) and a second during the body of the PETM (~0.8‰). In the Rin section, the PETM is characterised by a negative carbon isotope excursion of 2.8‰. The clays consist mostly of illite/smectite, illite, kaolinite, and chlorite consistent with a seasonal climate in the region, and we find a positive  $\delta^7\text{Li}_{\text{clays}}$  excursion of ~0.8‰.

The combined  $\delta^7\text{Li}_{\text{clays}}$  and  $\epsilon_{\text{Nd}}$  records indicate increased clay formation and increased silicate weathering fluxes in the semi-arid Pyrenees, while the sediment provenance was stable. The  $\delta^7\text{Li}$  values in the carbonate nodules indicate more variability, potentially due to clay contamination. Constrained by the bedrock type of dominantly reworked sediments and the seasonal precipitation regime, the initially low weathering fluxes, despite a comparatively high weathering intensity, evolved towards higher weathering fluxes with enhanced erosion during the PETM.

## Short Summary

How do semi-arid landscapes respond to rapid global warming? During the PETM – an extreme warming event 56 Ma ago – global lithium isotope records show a negative  $\delta^7\text{Li}$  excursion, suggesting an increase in weathering fluxes. In the Southern Pyrenees, however, we find the opposite signal: clay  $\delta^7\text{Li}$  values became ~1‰ heavier, indicating enhanced clay formation. These results suggest that regional hydroclimatic conditions can decouple terrestrial signals from global averages.

Formatted: Space Before: 0 pt

Deleted: ¶

Formatted: Font: Symbol

Formatted: Superscript

Deleted: , and efficient negative feedback

Deleted: despite stable sediment provenance

53 **1. Introduction**

54

55 Continental silicate weathering is a critical feedback mechanism that stabilises Earth's climate over geological  
56 timescales by regulating atmospheric CO<sub>2</sub> through the long-term carbon cycle (Walker et al., 1981; Raymo and  
57 Ruddiman, 1992; Maher and Von Blanckenburg, 2023). Through the breakdown of silicate minerals, the transport  
58 of cations in river systems, and the precipitation and burial of carbonates in the ocean, silicate weathering  
59 sequesters atmospheric CO<sub>2</sub>, acting as a natural climate thermostat. Understanding how this process responds to  
60 abrupt climate change is essential for evaluating its capacity to modulate carbon fluxes under a range of future  
61 warming scenarios.

62

63 The Palaeocene-Eocene Thermal Maximum (PETM), a hyperthermal event ~56 Ma ago, resulted from the rapid  
64 release of greenhouse gases that triggered a 5–8 °C global temperature increase over a geologically brief interval  
65 (Kennett and Stott, 1991; Dickens et al., 1995; Zachos et al., 2003, 2008; Westerhold et al., 2009; McNerney and  
66 Wing, 2011). Global records from the PETM suggest increases in silicate weathering fluxes (e.g. Hessler et al.,  
67 2017; Pogge von Strandmann et al., 2021; Jaimes-Gutierrez et al., 2025; Rush et al., 2025), while some local  
68 records have been interpreted to show increased weathering intensity (e.g. Ramos et al., 2022; Chen et al., 2023),  
69 underscoring the potential for weathering to buffer atmospheric CO<sub>2</sub> during extreme warming events. In the  
70 context of modern anthropogenic warming, these insights are crucial for understanding the capacity of natural  
71 systems to mitigate rising CO<sub>2</sub> levels (Zeebe et al., 2016; Carmichael et al., 2017 and references therein).

72

73 In mid-latitude records, a range of sedimentological, geochemical, and mineralogical proxies suggest that the  
74 PETM resulted in a hydrological perturbation with episodic extreme rainfall events, increased seasonality, and  
75 aridification, leading to a loss of vegetation, extreme flooding, and enhanced channel mobility (Schmitz et al.,  
76 2001; Schmitz and Pujalte, 2007; Carmichael et al., 2017; Chen et al., 2018; Rush et al., 2021; Barefoot et al.,  
77 2022; Vimperc et al., 2023). These changes were particularly pronounced in semi-arid regions such as the  
78 Southern Pyrenees (~35°N paleolatitude, **Fig. 1**), where sedimentary records document hydrological seasonality,  
79 enhanced erosion, and increased sediment transport (Schmitz and Pujalte, 2007; Pujalte et al., 2015; Chen et al.,  
80 2018; Rush et al., 2021; Prieur et al., 2024, 2025; Jaimes-Gutierrez et al., 2024).

81

82 The Southern Pyrenees (**Fig. 1**) offer an exceptional setting for investigating climate-driven weathering dynamics.  
83 This region experienced tectonic quiescence during the PETM (Rosenbaum et al., 2002), allowing for the isolation  
84 of the effects of climate and hydrology on weathering. Sedimentary records indicate enhanced hydrological  
85 seasonality and increased runoff, consistent with amplified denudation rates during this interval (Schmitz and  
86 Pujalte, 2007; Pujalte et al., 2015; Rush et al., 2021). In this study, we use lithium isotopes ( $\delta^7\text{Li}$ ) as a proxy for  
87 silicate weathering and neodymium isotopes ( $\epsilon_{\text{Nd}}$ ) as a tracer for sediment provenance, in order to quantify the  
88 weathering responses in the Southern Pyrenees and to assess their regional contribution to CO<sub>2</sub> regulation during  
89 the PETM.

90

91 We focus on two continental floodplain sections to answer two primary questions: (i) What was the chemical  
92 weathering response to the PETM in the semi-arid Southern Pyrenees? (ii) How do different sedimentary archives,  
93 such as clays and carbonate nodules, record the weathering changes? In the Esplugafreda section, we measured  
94  $\delta^7\text{Li}$  values in clay minerals as a weathering proxy, together with  $\epsilon_{\text{Nd}}$  values in two clay size fractions to determine  
95 sediment provenance. In the Rin section, we characterised the PETM locally through  $\delta^{13}\text{C}$  measurements in  
96 organic matter, and analysed the clay mineralogy of paleosols, and  $\delta^7\text{Li}$  values in both clays and carbonate  
97 nodules. These geochemical and mineralogical datasets allow us to reconstruct weathering dynamics in the region  
98 and to assess how they compare with existing globally-distributed records of PETM weathering (Pogge von  
99 Strandmann et al., 2021b; Ramos et al., 2022; Chen et al., 2023; Jaimes-Gutierrez et al., 2025a; Rush et al., 2025).

Deleted: was related to

Formatted: French (Switzerland)

Field Code Changed

Field Code Changed

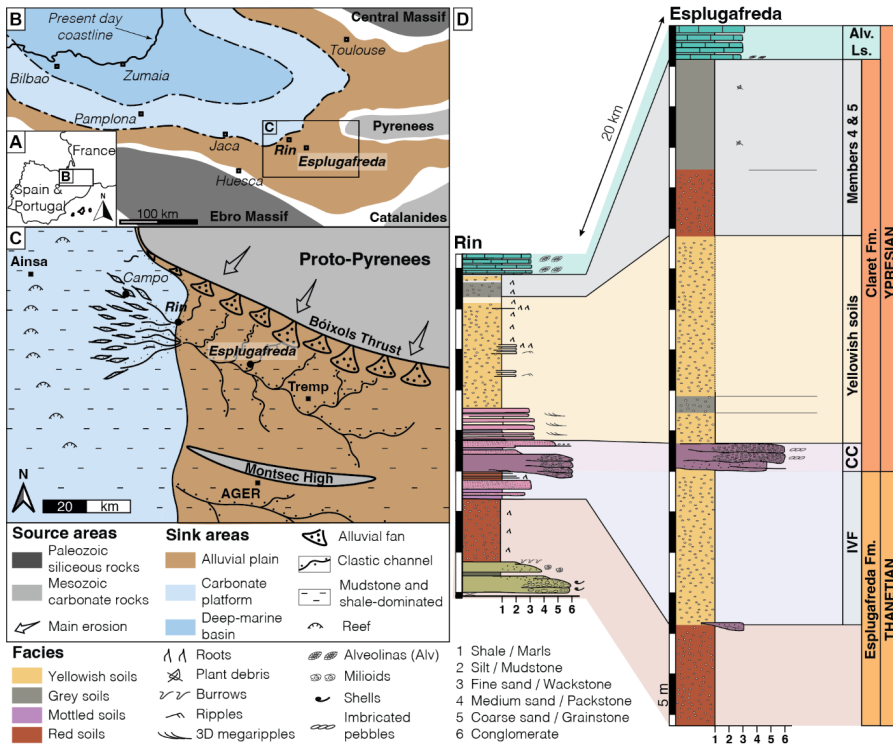
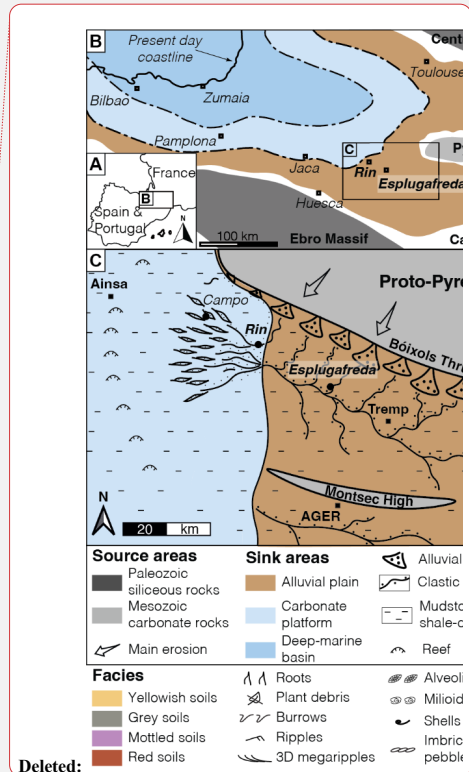


**Figure 1.** (A) Location map. (B) Palaeogeography of the Tremp-Graus Basin during the late Palaeocene, modified after Jaimes-Gutierrez et al. (2024) and references therein. (C) Sediment routing system during the late Palaeocene, with the floodplain Esplugafreda section and the more coastal Rin section, at the marine-continent transition, modified from Prieur et al. (2025). (D) Stratigraphy and correlation between the Esplugafreda and Rin terrestrial sections. CC, Claret Conglomerate. Alv. Ls., Alveolina Limestone.

### 1.1. Silicate weathering as Earth's surface thermostat

Silicate weathering rates are influenced by climate (Dessert et al., 2003; West et al., 2005), vegetation (Moulton et al., 2000; Porder, 2019), lithology (Dessert et al., 2003; Caves et al., 2016; Murray and Jagoutz, 2024), and regolith properties (Kump and Arthur, 1997; Caves Rügenstein et al., 2019). Weathering is driven by the availability of fresh mineral surfaces, reactive fluids, and dissolution kinetics (Riebe et al., 2004; Bufer et al., 2021; Maher and Von Blanckenburg, 2023). Denudation ( $D = \text{erosion rate } [E] + \text{silicate weathering } [W]$ ) links surface processes to the carbon cycle because erosion supplies fresh minerals, enhancing  $\text{CO}_2$  sequestration through chemical weathering (Gaillardet et al., 1999; Riebe et al., 2004; West et al., 2005; Anderson et al., 2007; Hilton, 2023).

Two end-member regimes can be used to describe chemical weathering dynamics. In supply-limited regimes, mature soils dominated by secondary clays shield bedrock, limiting fresh mineral exposure and resulting in low weathering rates (Goddéris et al., 2008). In kinetically-limited regimes, which are typical of high-relief areas with thin soils, weathering rates are controlled by mineral dissolution kinetics (Kump et al., 2000; Riebe et al., 2004; West et al., 2005). Investigating how climate and erosion interact to shape these regimes under hyperthermal events such as the PETM is thus essential for understanding the weathering mechanisms and rates underpinning Earth's carbon cycle feedbacks in a warming climate.



Deleted:

124 **1.2. Lithium isotopes as a chemical weathering tracer**

125 Secondary clay minerals, which form as a by-product of primary silicate rock dissolution, preferentially  
126 incorporate  $^6\text{Li}$  over  $^7\text{Li}$ , resulting in isotopically light clays and isotopically heavy waters (e.g. Pogge von  
127 Strandmann et al., 2020). As weathering progresses, both dissolved lithium and the clays that precipitate from it  
128 become isotopically heavier, with the  $\delta^7\text{Li}$  value of the water and soil being linked by an approximately constant  
129 fractionation factor (Pogge von Strandmann et al., 2021a). Measuring  $\delta^7\text{Li}$  values in detrital and carbonate  
130 archives therefore allows past weathering regimes to be reconstructed. Because carbonate weathering has a  
131 minimal influence on riverine lithium budgets,  $\delta^7\text{Li}$  variations primarily reflect silicate weathering processes  
132 (Kısakürek et al., 2005). Consequently, lithium isotopes have become widely applied as a proxy for tracking clay  
133 mineral formation, and thereby tracing silicate weathering intensity changes, both in modern systems (e.g.  
134 Dellinger et al., 2015, 2017; Pogge von Strandmann et al., 2023) and during past geological events (e.g. Misra  
135 and Froelich, 2012; Pogge von Strandmann et al., 2013, 2021; Ramos et al., 2022; Jones et al., 2023).

136  
137 Weathering congruency, which represents the balance between primary mineral dissolution and secondary clay  
138 mineral formation, determines the  $\delta^7\text{Li}$  composition of river waters and sediments (Dellinger et al., 2015; Zhang  
139 et al., 2022 and references therein). In rapidly eroding regions with low  $W/D$ , congruent weathering results in  
140 minimal isotopic fractionation, because clay formation is relatively low (Fig. 2). In contrast, incongruent  
141 weathering in soil-mantled environments with moderate  $W/D$ , such as floodplains with high clay formation, yields  
142 both clays and waters with higher  $\delta^7\text{Li}$  values (Fig. 2 and 3). Finally, in supply-limited regimes with high  $W/D$ ,  
143 such as rainforests, there is no remaining primary rock material to weather, so pre-formed clays are re-dissolved,  
144 which drives solutions to low  $\delta^7\text{Li}$  values, but with a very low weathering flux (e.g. Dellinger et al., 2015). In  
145 modern rivers, clays take up their Li from solution with an approximately constant fractionation factor (Pistiner  
146 and Henderson, 2003; Pogge von Strandmann et al., 2023; Ramos et al., 2024), so their composition also mimics  
147 this boomerang curve (Winnick et al., 2022; Pogge von Strandmann et al., 2023; Wei et al., 2025).

148  
149 In detrital sediment archives, only part of this boomerang trend is typically observed because of mixing of the  
150 neoformed clays with primary silicate material, especially at low  $W/D$  conditions (Dellinger et al., 2017).  
151 Therefore, continental and marine detrital records may need to be interpreted differently (e.g. Pogge von  
152 Strandmann et al., 2021; Ramos et al., 2022, 2024; Jones et al., 2023; Jaimes-Gutierrez et al., 2025; Rush et al.,  
153 2025; Wei et al., 2025). Because finer sediment fractions tend to be preferentially transported further offshore due  
154 to hydrodynamic sorting during river to marine transport, clay-sized records may be more clearly expressed in  
155 some marine sedimentary records (e.g. Gibbs, 1977; Liu et al., 2023). Such biases resulting from mixing with  
156 primary silicate grains in bulk sediment samples can potentially be reduced by analysing the clay size fraction ( $<2$   
157  $\mu\text{m}$ ), although this fraction can still also contain some primary minerals.

158  
159 Finally, lithium isotopes can also be fractionated by direct climatic fluctuations. For example, temperature (Vigier  
160 et al., 2008; Li and West, 2014) and hydrological controls (Zhang et al., 2022) have both been found to influence  
161 the  $\delta^7\text{Li}$  composition of river water, and consequently the composition of the sedimentary archives that form in  
162 equilibrium with them (Pogge von Strandmann et al., 2023). In particular, riverine dissolved  $\delta^7\text{Li}$  values have  
163 been shown to have a negative correlation with runoff, because it controls the water-rock residence time that  
164 affects clay formation, with the dry season exhibiting enhanced clay formation and higher  $\delta^7\text{Li}$  values than the  
165 wet season (Wilson et al., 2021; Zhang et al., 2022).

166  
167 A detailed discussion on the lithium isotope interpretative framework, including the roles of grain size,  
168 hydrodynamic sorting, and lithology, is provided in Jaimes-Gutierrez et al. (2025, Supplemental Material).

169

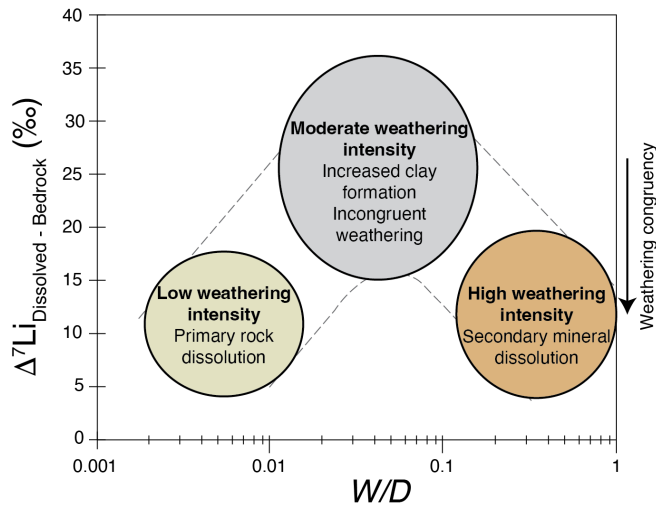
Formatted: German

Field Code Changed

Formatted: No underline, French (Switzerland)

Formatted: No underline, French (Switzerland)

Field Code Changed



170  
 171 **Figure 2.** Large-river dissolved lithium isotope composition ( $\delta^7\text{Li}_{\text{dissolved}}$ ) corrected for bedrock composition  
 172 ( $\Delta^7\text{Li}_{\text{dissolved-bedrock}}$ ) plotted versus weathering intensity ( $W/D$ ). Modified from Dellinger et al. (2015) and references  
 173 therein.  
 174

175 During the PETM, Pogge von Strandmann et al. (2021) documented a  $\sim 3\%$  negative  $\delta^7\text{Li}$  excursion in several  
 176 marine carbonate sections, indicating globally enhanced weathering fluxes (50–60%) and erosion rates (2–3x),  
 177 and a shift to an overall lower weathering intensity regime. At a continental scale, detrital lithium isotope records  
 178 from North America show coherent negative  $\delta^7\text{Li}$  excursions in both floodplain and deep-marine settings,  
 179 indicating rapid propagation of erosion- and weathering-related signals through sediment-routing systems under  
 180 intensified hydrological conditions, despite largely stable sediment provenance (Ramos et al., 2022; Jaimes-  
 181 Gutierrez et al., 2025a; Rush et al., 2025). On a regional scale, Ramos et al. (2022) reported a rapid, sustained  
 182 increase in silicate weathering intensity in the Bighorn Basin floodplains that was attributed to seasonal  
 183 hydrological variability. Similarly, Chen et al. (2023) identified a  $\sim 100\%$  increase in silicate weathering intensity  
 184 in the Nanyang Basin, East Asia. These studies highlight the roles of local hydrology, lithology, and erosion in  
 185 shaping regional weathering responses and the associated  $\delta^7\text{Li}$  changes. However, they also reveal significant  
 186 gaps in our understanding of how regional processes integrate into driving global  $\delta^7\text{Li}$  records and carbon cycle  
 187 feedbacks. Notably, discrepancies between the proposed increases in weathering intensity at a regional scale  
 188 (Ramos et al., 2022; Chen et al., 2023) and the inferred decrease at a global scale (Pogge von Strandmann et al.,  
 189 2021b; Jaimes-Gutierrez et al., 2025a; Rush et al., 2025) require further assessment of how regional climatic and  
 190 geological controls translate into weathering responses.  
 191

Formatted: French (Switzerland)

Field Code Changed

Formatted: French (Switzerland)

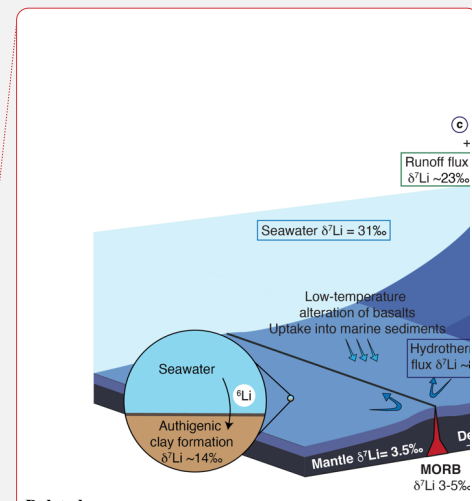
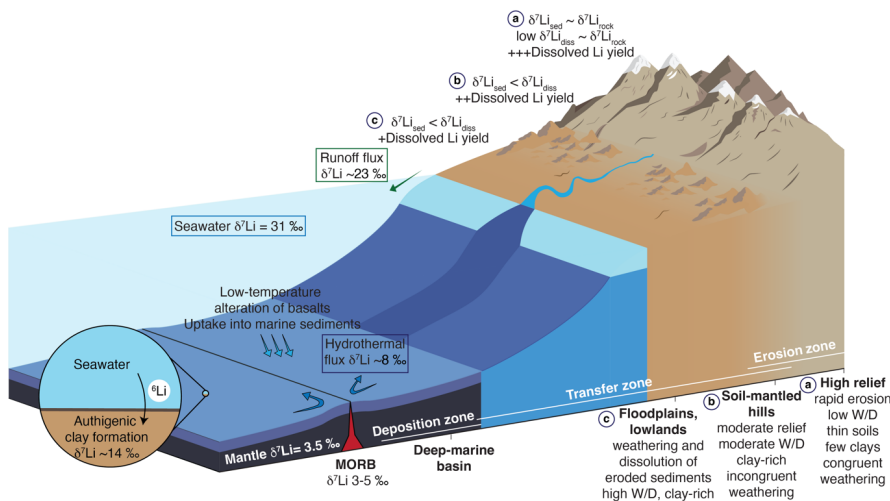


**Figure 3.** Processes determining the lithium isotope composition of bulk sediments ( $\delta^{7}\text{Li}_{\text{sed}}$ ) and dissolved lithium flux along a sediment routing system from source to sink in relation to denudation. The weathering intensity ( $W/D$ ) expresses the relative share of weathering ( $W$ ) over denudation ( $D$ ), where  $D = W + E$  (erosion). Modified from Tofelde et al. (2021), Pogge von Strandmann et al. (2021a), and Bufer et al. (2024).

To address these gaps, we focused on the silicate weathering response to the PETM climatic perturbation in two sections of the Southern Pyrenees (Espugafreda and Rin, Fig. 1). With its semi-arid climate, seasonal precipitation, and relatively unreactive lithologies comprising reworked sediments and significant carbonate content (e.g. Eichenseer, 1988; Eichenseer and Luterbacher, 1992; Gómez-Gras et al., 2016), this setting represents a contrasting regional weathering regime to previous PETM studies. Our results contribute to understanding how floodplain paleosols, which are often overlooked in global weathering studies, respond to climatic perturbations, with broader implications for the recovery of Earth's climate system after significant warming events.

## 2. Geological context

The Pyrenees formed as a result of convergence between the Iberian and European plates, a process that initiated in the Late Cretaceous and continued into the Miocene (Mattauer and Henry, 1974; Roure et al., 1989; Roest and Srivastava, 1991; Rosenbaum et al., 2002). The orogenic evolution began with the mid-Cretaceous hyper-extension of the Iberian margins, followed by the late Cretaceous subduction and collision with the European plate (Teixell et al., 2016). Foreland basins formed on both sides of the fold and thrust belt (Puigdefregas and Souquet, 1986; Muñoz, 1992; Gómez-Gras et al., 2016). The Southern Pyrenean foreland basin was active between the Late Cretaceous and the Oligocene, and contains well-preserved sedimentary archives of continental and marine environments.

The Tremp-Graus Basin is located in the South-Central Pyrenean Foreland Basin (Spain), delimited by the Boixols Thrust to the north and the Montsec Thrust to the south (Fig. 1C). During the Palaeocene, the Tremp-Graus Basin was dominated by continental sedimentation sourced from the Pyrenees (Gómez-Gras et al., 2016). The continental deposits of the Thanetian Esplugafreda Formation (Fm.) predominantly represent floodplain sediment accumulation and consist of clay, silt, carbonate nodules, and Microcodium grains, with some isolated sandy to conglomeratic channels (Puigdefregas and Souquet, 1986; Dreyer, 1993; Schmitz and Pujalte, 2003, 2007).

### 2.1. Esplugafreda section

The Esplugafreda section (42°14'50" N; 0°45'13" E, Fig. 1B) has been widely studied for its well-preserved Palaeocene-Eocene sedimentary record (Schmitz and Pujalte, 2003; Baceta et al., 2005; Khozyem, 2013; Tremblin et al., 2022; Basilici et al., 2022; Jaimes-Gutierrez et al., 2024) (Fig. 1D). The Upper Thanetian sediments belong to the Esplugafreda Fm. in the Tremp Group of the Tremp-Graus Basin (Dreyer, 1993). This formation consists of coarse-grained stream deposits intercalated with red floodplain sediments that are rich in carbonate nodules and characterised by mature paleosols. The PETM sediments have been classified into five stratigraphic members

229 (Pujalte and Schmitz, 2005; Pujalte et al., 2014; Colombera et al., 2017; Basilici et al., 2022). Member 1 belongs to the Esplugafreda Fm. and consists of a fining-upwards sequence of conglomerates and cross-laminated sandstones, known as the Incised Valley Fill (IVF) sediments. During this interval, a first negative carbon isotope excursion (CIE) marks the Pre-Onset Excursion (POE) (Khozyem, 2013; Tremblin et al., 2022). Member 2 at the onset of the Ypresian is represented by the Claret Conglomerate (Pujalte and Schmitz, 2005), a 3-5 m thick conglomeratic unit, corresponding to a braid plain which has been interpreted as the proximal part of a megafan (Schmitz and Pujalte, 2007). Member 3, the Yellowish soils, consists of yellow mudstone with purple mottling, and the main body of the CIE is recorded during this interval (Pujalte and Schmitz, 2005). Member 4, consisting of red soil with gypsum, and Member 5, comprising light red mudstones with scarce carbonate nodules, correspond to the recovery interval of the PETM in this locality (Pujalte and Schmitz, 2005; Baceta et al., 2011; Khozyem, 2013; Pujalte et al., 2014; Tremblin et al., 2022; Basilici et al., 2022).

## 240 2.2. Rin section

241 The Rin section (42°19'42.01"N; 0°32'42.16"E, **Fig. 1B** and **Fig. 4**) is a Palaeocene-Eocene sequence comprising mudstone-dominated alluvial deposits and very shallow marine carbonate alternations, indicating episodes of transgression and regression on the coastal plain (Schmitz and Pujalte, 2007) (**Fig. 1**). The upper Esplugafreda Fm. soils are characterised by grey mottling and sparse iron nodules, with preserved pedogenic features such as peds. Member 1, the IVF, consists of 4 m-thick reddish-yellow soils that are rich in carbonate nodules. Member 2, the Claret Conglomerate, outcrops as a 3 m-thick calcareous conglomerate with pale red clay pockets, and has sparse carbonate nodules and charophyte occurrences. Member 3, the Yellowish soils, consists of 13 m-thick reddish-yellow clays and silts. The base of Member 3 records sparse occurrences of lignite and carbonate nodules. Member 4 is not preserved in the Rin section, and the upper 3 m of the sequence consists of Member 5, which has light grey to reddish yellow soils with grey mottling, before the overlying Alveolina Limestone.



252 **Figure 4.** Rin section between the upper Thanetian and lower Ypresian. Members 1-5 described in the literature for the Esplugafreda section can be identified in the Rin section, except that Member 4 from the recovery phase of the PETM has not been preserved. E. Fm.: Esplugafreda Formation.

## 256 3. Material and methods

### 257 3.1. Size fraction separation

258 Standard protocols (e.g. Adatte et al., 1996; Bauer et al., 2016) were followed for decarbonation and size fraction separation at the Institute of Earth Sciences clay laboratory at the University of Lausanne (ISTE-UNIL). Samples (~5 g) were leached with 10% HCl for 30 min in a bubble bath, including 3 min in an ultrasonic bath, to disaggregate sediments and dissolve calcite. Distilled water was used to remove the acid until a neutral pH was obtained. Subsequently, the <2 μm fraction was separated by settling and enhanced with a centrifuge. Settling and extraction were repeated three times.

### 264 3.2. Clay mineralogy

265 The clay minerals were identified on air-dried and ethylene glycol-solvated samples at ISTE-UNIL following the protocol described in Adatte et al. (1996). An aliquot of the separated size fractions was pipetted on glass slides and dried at room temperature. The air-dried samples were further analysed with a Thermo Scientific ARL X'TRA powder diffractometer equipped with a Cu anode, operated at 45 kV and 40 mA. The step size was 0.02° with a scan rate of 0.5-1.2°/min. Samples were glycolated to identify smectite (Moore and Reynolds, 1992). Diffractograms were analysed using the XRDWin software, where the background was removed, and a deconvolution was performed for overlapping peaks (e.g. K002 and Ch004).

Formatted: English (US)

Formatted: English (US)

### 272 3.3. Nodule purification

273 Carbonate nodules were washed with running distilled water until visible clay clumps were removed. They were  
274 then placed in a beaker with distilled water and in an ultrasonic bath to remove the remaining clay particles. A  
275 second round in the ultrasonic bath was then carried out with some drops of 10 M HCl in order to remove the  
276 outermost layer. The nodules were later washed in running distilled water, dried at 40 °C, and ground.

Formatted: English (US)

### 277 3.4. Rock-Eval pyrolysis

278 Organic matter analyses were performed on powdered bulk rock samples using a Rock-Eval 6 at ISTE-UNIL,  
279 following standard methodology (Espitalie et al., 1985; Behar et al., 2001). For calibration, the IFP 160000  
280 standard was used. The Rock-Eval pyrolysis parameters measured were hydrogen index (HI, mg HC/g TOC, HC  
281 = hydrocarbons), oxygen index (OI, mg CO<sub>2</sub>/g TOC), Tmax (°C), and total organic carbon content (TOC, wt.%).  
282 The HI, OI, and Tmax values give an overall measurement of the type and degree of maturation of the organic  
283 matter (e.g. Espitalie et al., 1985).

Formatted: Subscript

### 284 3.5. Isotope geochemistry

#### 285 3.5.1. Organic matter carbon isotopes

286 The carbon isotope composition of the decarbonated bulk rock samples was determined at the Institute of Earth  
287 Surface Dynamics at the University of Lausanne (IDYST-UNIL) by elemental analysis/isotope ratio mass  
288 spectrometry (EA/IRMS). The EA/IRMS system consisted of a Carlo Erba 1108 (Fisons Instruments, Milan, Italy)  
289 elemental analyser connected to a Delta V Plus isotope ratio mass spectrometer via a ConFlo III split interface  
290 (both Thermo Fisher Scientific, Bremen, Germany) operated under continuous helium (He) flow (Spangenberg,  
291 2006; Spangenberg and Zufferey, 2019). The carbon isotope compositions were reported in the delta (δ) notation  
292 as permil (‰) variations of the molar ratio of the heavy to light isotope (<sup>13</sup>C/<sup>12</sup>C) relative to the international  
293 standard Vienna Pee Dee Belemnite limestone (VPDB). For calibration and normalisation of the measured δ<sup>13</sup>C  
294 values to the Vienna Pee Dee Belemnite limestone (VPDB) standard, a four-point calibration was used with  
295 international reference materials and in-house standards (Spangenberg and Zufferey, 2019). The used standards  
296 included UNIL-Glycine (δ<sup>13</sup>C = -26.10 ± 0.05‰), UNIL-Urea-1 (δ<sup>13</sup>C = -43.00 ± 0.04‰), UNIL-Pyridine (δ<sup>13</sup>C  
297 = -29.25 ± 0.06‰), and the RM USGS24 graphite (δ<sup>13</sup>C = -16.05 ± 0.04‰). Analyses were done in duplicates.  
298 The accuracy of the analyses was checked periodically through the analysis of international RM standards not  
299 used for calibration. The reproducibility and precision of the EA/IRMS δ<sup>13</sup>C analyses were determined by the  
300 standard deviation of separately replicated analyses and were better than 0.1‰.

#### 301 3.5.2. Lithium isotopes

302 Sample digestion, column chemistry, and mass spectrometry were conducted in the London Geochemistry and  
303 Isotope Centre (LOGIC) laboratories at University College London (UCL) and Birkbeck, University of London.  
304 Clay samples were subjected to bulk digestion using concentrated HF, HNO<sub>3</sub>, and HClO<sub>4</sub> in Teflon beakers on a  
305 hot plate at 130 °C, followed by steps in concentrated HNO<sub>3</sub> and 6 M HCl. The carbonate nodules were subject  
306 to leaching to separate the carbonate and detrital fractions. The carbonate fraction was extracted by leaching ~100  
307 mg of sample in 8 ml 0.1 M HCl for 1 h (Pogge von Strandmann et al., 2013; Wilson et al., 2021), allowing a  
308 maximum of ~40 mg of calcium carbonate to be dissolved.  
309

310 A standard method of elution was applied for lithium isotope separation in 0.2 M HCl. Two-column passes were  
311 applied through AG50W-X12 resin to ensure matrix removal (Pogge von Strandmann et al., 2013). Given that  
312 lithium isotopes are fractionated during ion chromatography, sample splits were collected before and after the  
313 lithium collection interval to assess column yields. For example, a 1% loss in yield at UCL has been assessed to  
314 lead to an offset of 1.7‰ (Wilson et al., 2021). Here, yields between two column passes were 99.8-100%,  
315 indicating excellent recovery.  
316

317 Lithium isotope measurements were performed on a Nu Plasma 3 MC-ICP-MS at UCL, using a Cetac Aridus 2  
318 desolvation system, 'super-lithium' cones, and standard-sample bracketing with the IRMM-016 Li standard  
319 (Pogge von Strandmann et al., 2019). Samples were measured at least three times within an analytical session,  
320 with each measurement integrating ~50 s, and the reported values are the mean and standard deviation (2sd)  
321 of these values, given in permil (‰) relative to the IRMM-016 standard. Accuracy and external reproducibility were  
322 assessed using seawater and USGS standard BCR-2, which gave δ<sup>7</sup>Li values of +31.3 ± 0.6‰ (2sd, n = 28) and  
323 +2.5 ± 0.3‰ (n = 5), respectively.

### 324 3.5.3. Neodymium isotopes and rare earth element concentrations

325 After decarbonation using 10% HCl for 30 min, clays were separated from decarbonated sediments into <0.5 µm  
326 and 0.5-2 µm fractions (analytical protocol for size fraction separation reported in Jaimes-Gutierrez et al., 2024).  
327 A total of 18 samples (8 in the <0.5 µm size fraction and 10 in the 0.5-2 µm size fraction) were analysed for their  
328 neodymium (Nd) isotopic composition and their Nd and samarium (Sm) concentrations. Aliquots of about 1.5 mg  
329 of each clay fraction followed a sequential leaching procedure to remove Fe-Mn oxides and organic matter, based  
330 on the protocol of Bayon et al. (2002) and Gutjahr et al. (2007), slightly adapted. The Fe-Mn oxides were removed  
331 using a solution of 0.5 M hydroxylamine hydrochloride in 20% v/v acetic acid for 48h. Then, the organic matter  
332 was removed with a 5% H<sub>2</sub>O<sub>2</sub> solution for 48h.

333  
334 The leached samples were dried and digested by alkaline fusion following the protocol of Bayon et al. (2009),  
335 along with certified standards (BHVO-2, BRC-2) from the United States Geological Survey (USGS).  
336 Approximately 50 mg of each sample underwent alkaline fusion in a carbon crucible with 0.6 g of NaOH and 1.2  
337 g of Na<sub>2</sub>O<sub>2</sub> heated at 650°C for 12 min in a furnace, before adding ultrapure water in which Fe-hydroxides  
338 precipitated, concentrating rare earth elements. After centrifugation, the samples were dissolved in 3 ml 4 M HCl.

339  
340 From this solution, an aliquot of 0.3 ml was extracted for analyses of Nd and Sm concentrations. Part of the  
341 samples were measured for their Nd and Sm concentrations on an Agilent 7500 quadrupole ICP-MS spectrometer  
342 in the Laboratoire Magmas et Volcans (LMV) in Clermont-Ferrand (France), and quantified using standard  
343 bracketing with a solution of BHVO-2 during the session. Accuracy and reproducibility were assessed using two  
344 BHVO-2 and one BCR-2 samples among the samples. Deviations of Nd and Sm concentrations from these  
345 standards were below 11%. The other part of the samples was measured for their Nd and Sm concentrations on a  
346 Thermo Scientific X-Series II® at the Pole Spectrométrie Océan in Brest (France), and quantified using multi-  
347 element calibration standards prepared from single element standards purchased from SCP science (Baie d'Urfé,  
348 Québec, Canada). Accuracy and reproducibility were assessed using one BHVO-2 and one BCR-2 sample, which  
349 were analysed among the samples. Deviations of Nd and Sm concentrations from these standards were below 7  
350 %.

351  
352 Purified neodymium fractions were isolated from the mother solution by ion chromatography following the  
353 protocol described in Gaitan et al. (2023) for the low-pressure, automated column chromatography PrepFAST-  
354 MC® system device, using AG50W-X8 (200-400 mesh) resin for rare earth element separation and Ln Spec (50-  
355 100 µm) resin for Nd separation. Part of the neodymium isotopic measurements was performed on a MC-ICP-MS  
356 Neptune Plus (Thermo Scientific) at the Laboratoire Magmas et Volcans in Clermont-Ferrand (France). Ratios  
357 were corrected for mass bias using an exponential law and a <sup>143</sup>Nd/<sup>144</sup>Nd ratio of 0.7219. Mass-bias-corrected  
358 <sup>143</sup>Nd/<sup>144</sup>Nd were normalised to a JNdi-1 value of 0.512115 (Tanaka et al., 2000). Repeated measurements of  
359 JNdi-1 throughout the session gave an external reproducibility of ± 0.000009 (2σ, n = 15), corresponding to ±  
360 0.18 in the standard ε<sub>Nd</sub>(0) notation. Analyses of two BHVO-2 reference materials yielded a <sup>143</sup>Nd/<sup>144</sup>Nd ratio of  
361 0.512991 ± 0.000005 for each, in excellent agreement with the published value of 0.512990 ± 0.000010 (Weis et al.,  
362 2005). The other part of the samples was analysed on an MC-ICP-MS Neptune Plus (Thermo Scientific) at the  
363 ENS of Lyon (France). Ratios were corrected for mass bias using an exponential law and a <sup>143</sup>Nd/<sup>144</sup>Nd ratio of  
364 0.7219. Mass-bias-corrected <sup>143</sup>Nd/<sup>144</sup>Nd values were normalised to a JNdi-1 value of 0.512115 (Tanaka et al.,  
365 2000). Repeated measurements of JNdi-1 throughout the session gave an external reproducibility of ± 0.000018  
366 (2σ, n = 16), corresponding to ± 0.34 in the standard ε<sub>Nd</sub>(0) notation. Analyses of four BHVO-2 reference materials  
367 gave an average <sup>143</sup>Nd/<sup>144</sup>Nd ratio of 0.512985 ± 0.000009 for each, in agreement with the published value of  
368 0.512990 ± 0.000010 (Weis et al., 2006).

369  
370 The data are reported in the standard epsilon notation ε<sub>Nd</sub> = [((<sup>143</sup>Nd/<sup>144</sup>Nd)<sub>sample</sub> / (<sup>143</sup>Nd/<sup>144</sup>Nd)<sub>CHUR</sub>) - 1] \* 10<sup>4</sup>,  
371 corrected for the radioactive decay of <sup>147</sup>Sm to <sup>143</sup>Nd based on the Nd and Sm concentrations measured for each  
372 sample (<sup>147</sup>Sm/<sup>144</sup>Nd = Sm/Nd \* 0.6049), an age of 55.8 Ma, and the <sup>147</sup>Sm radioactive decay constant λ (6.54 ×  
373 10<sup>-12</sup> y<sup>-1</sup>; Lugmair & Marti, 1977). The CHUR (CHondritic Uniform Reservoir) <sup>143</sup>Nd/<sup>144</sup>Nd ratio was also  
374 corrected using a <sup>147</sup>Sm/<sup>144</sup>Nd ratio of 0.1960 and a present-day value of 0.512630 (Bouvier et al., 2008).

## 376 4. Results

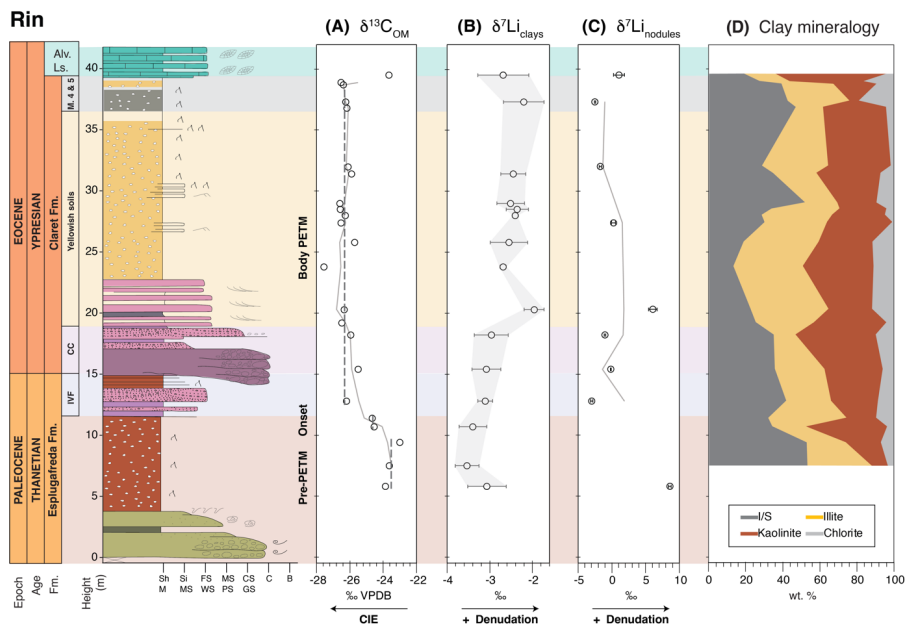
### 377 4.1. Clay mineralogy in the Rin section

378 The clay mineralogy in the Rin section (Fig. 5D, Table S1) comprises mixed-layer illite-smectite (I/S), with a  
379 mean abundance of 34 ± 11 (1σ) wt.%; illite, 29 ± 9 wt.%; kaolinite, 30 ± 11 wt.%; and minor chlorite, 7 ± 5  
380 wt.%. The pre-PETM samples have a mixed-layer I/S abundance of 42 ± 10 wt.%, decreasing to 32 ± 10 wt.%

381 during the body of the PETM. The kaolinite abundance increases from  $22 \pm 14$  wt.% to  $32 \pm 9$  wt.% during the  
 382 PETM body, while the illite and chlorite abundances remain stable.

383 **4.2. Organic matter carbon isotopes in the Rin section**

384 Throughout the section, the mean  $\delta^{13}\text{C}_{\text{OM}}$  value is  $-25.7\text{‰}$ , with a standard deviation ( $1\sigma$ ) of  $1.2\text{‰}$  (Fig. 5A, Table  
 385 S2). The pre-PETM samples, between 5.8 and 9.4 m, have a mean value of  $-23.5 \pm 0.5\text{‰}$ . A negative excursion  
 386 begins in samples at 10.7 and 11.4 m, with values decreasing to  $-24.6 \pm 0.1\text{‰}$ . The most depleted values occur  
 387 between 12.8 and 38.9 m, with a mean of  $-26.3 \pm 0.5\text{‰}$ . The final sample at 39.5 m, below the Alveolina  
 388 Limestone, suggests a return to pre-PETM levels, with a value of  $-23.7\text{‰}$ .  
 389



390 **Figure 5.** Rin section isotopes and clay mineralogy. (A) The  $\delta^{13}\text{C}_{\text{OM}}$  record shows the negative Carbon Isotope  
 391 Excursion (CIE), with an onset before the Claret Conglomerate and sustained negative values until the Alveolina  
 392 Limestone. (B) The CIE was accompanied by a positive excursion in lithium isotopes of the clays ( $\delta^7\text{Li}_{\text{clays}}$ ),  
 393 reaching a  $0.9\text{‰}$  excursion in the Yellowish soils member. (C) Lithium isotopes in the carbonate nodules showed  
 394 high variability and a less conclusive trend. (D) Rin section clay mineralogy. The pre-PETM and body intervals  
 395 were determined based on the  $\delta^{13}\text{C}_{\text{OM}}$  record and the stratigraphy. Dashed lines in panel A represent average  
 396 values for  $\delta^{13}\text{C}_{\text{OM}}$  in the pre-PETM and syn-PETM intervals. Grey bars in panel B outline the analytical  
 397 uncertainty ( $2\text{sd}$ ) of  $\delta^7\text{Li}_{\text{clays}}$ .  
 398

399 **4.3. Lithium isotopes in the Rin and Esplugafreda sections**

400 The clays of the Rin section have a mean lithium isotope composition of  $-2.9 \pm 0.5\text{‰}$  ( $1\sigma$ ) (Fig. 5B, Table S2).  
 401 Between 5.8 and 18.2 m, the mean composition is  $-3.4 \pm 0.2\text{‰}$ . Above this, from 20.3 to 39.5 m, the mean  
 402 composition is  $-2.6 \pm 0.2\text{‰}$ , which corresponds to a shift towards more positive values of  $\sim 0.8\text{‰}$ . The minimum  
 403 value of  $-3.7\text{‰}$  is seen before the Claret Conglomerate, and the maximum value of  $-2.2\text{‰}$  occurs immediately  
 404 after the Claret Conglomerate, indicating a total range of up to  $\sim 1.5\text{‰}$ . The  $\delta^7\text{Li}$  values measured on carbonate  
 405 nodules have a maximum value of  $8.6\text{‰}$ , a minimum value of  $-3.0\text{‰}$ , and a mean composition of  $0.9 \pm 4.0\text{‰}$   
 406 (Fig. 5C). No clear temporal trend is observed in the  $\delta^7\text{Li}_{\text{nodules}}$  record. No systematic correlation is observed  
 407 between  $\delta^7\text{Li}_{\text{clays}}$  and the relative abundance of individual clay minerals within analytical uncertainty (Fig. S1).  
 408

409 At the Esplugafreda section, the clays have a mean lithium isotope composition of  $-3.7 \pm 0.7\text{‰}$  (Fig. 6B, Table  
 410 S3). The pre-PETM samples (0-10 m and 21-28 m, Jaimes-Gutierrez et al., 2024 and references therein) have a

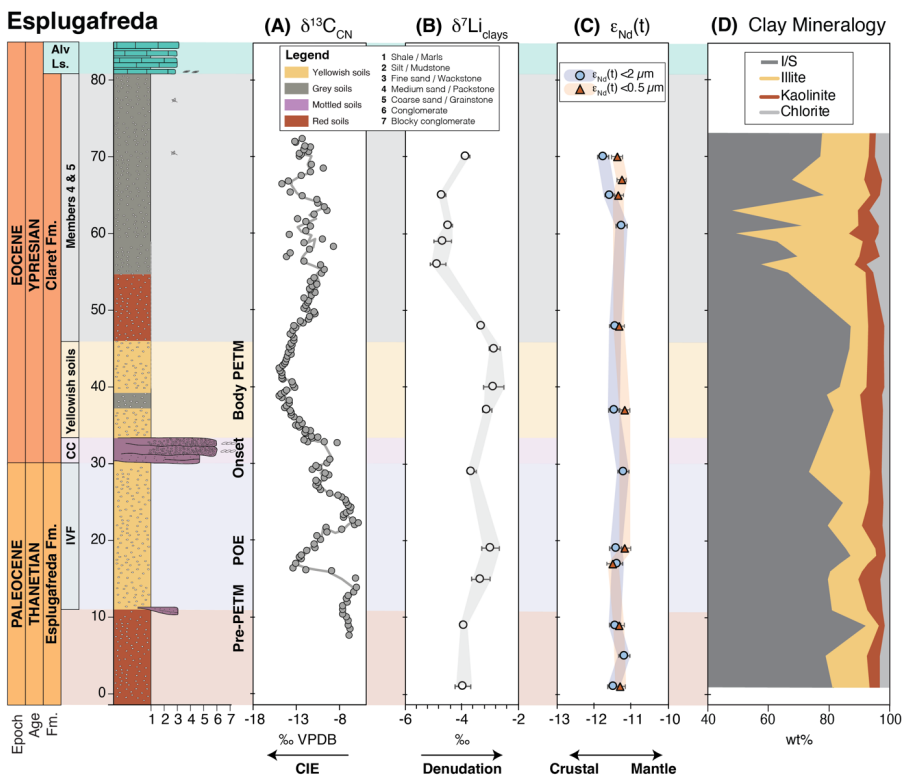
Deleted: , suggesting clay contamination  
 Deleted: Grey bars  
 Deleted: , and  
 Deleted: , grey bars  
 Deleted: they

416 mean composition of  $-3.8 \pm 0.2\%$ . The POE samples ( $\sim 15\text{--}21\text{ m}$ ) have a composition of  $-3.2 \pm 0.2\%$ , and the  
 417 syn-PETM sediments have a composition of  $-3.0 \pm 0.2\%$ , indicating a PETM shift towards more positive values  
 418 of  $\sim 0.8\%$ . The post-PETM sediments have a composition of  $-4.5 \pm 0.4\%$ . Samples from the pre-PETM, Pre-  
 419 Onset Excursion (POE), and syn-PETM intervals display relatively heavier  $\delta^7\text{Li}_{\text{clays}}$  values, whereas recovery-  
 420 phase samples form a distinct cluster characterised by lighter  $\delta^7\text{Li}_{\text{clays}}$  (Fig. S2).  
 421

#### 4.4. Neodymium isotopes in the Esplugafreda sections

423 Throughout the Esplugafreda section, the  $0.5\text{--}2\ \mu\text{m}$  clays have a mean  $\epsilon_{\text{Nd}}(t = 55.8\text{ Ma})$  composition of  $-10.94 \pm$   
 424  $0.16 (2\sigma)$ , while the  $<0.5\ \mu\text{m}$  fraction has a mean composition of  $-10.88 \pm 0.11$  (Fig. 6C, Table S4). In comparison,  
 425 the typical analytical uncertainty on any individual sample measurement was  $0.21 (2\sigma)$ . Hence, these values are  
 426 considered constant through time, with no deviation significantly outside the analytical uncertainty. The  
 427 neodymium isotope measurements on the  $<0.5\ \mu\text{m}$  fraction are also indistinguishable from those on the  $0.5\text{--}2\ \mu\text{m}$   
 428 fraction (Fig. 6C).  
 429

Formatted: Space Before: 0 pt



430  
 431 **Figure 6.** Esplugafreda section isotopes and clay mineralogy. (A) The  $\delta^{13}\text{C}$  record from microcrystalline  
 432 carbonate nodules (from Khozyem, 2013) shows a negative carbon isotope excursion during the Pre-Onset  
 433 Excursion (POE) and during the main body of the PETM. (B) Positive excursions in lithium isotopes of the clays  
 434 ( $\delta^7\text{Li}_{\text{clays}}$ ) during both the POE and the main CIE of the PETM. (C) Neodymium isotopes ( $\epsilon_{\text{Nd}}(t = 55.8\text{ Ma})$ ) show  
 435 no variation throughout the section, indicating constant provenance. (D) Esplugafreda section clay mineralogy  
 436 (modified from Jaimes-Gutierrez et al., 2024).

Deleted: There were p

## 5. Discussion

### 5.1. The PETM in the Rin section

439 The PETM sediments in the Rin section represent an archive of the climatic perturbation in a coastal terrestrial  
 440 setting (Pujalte et al., 2014; Prieur et al., 2025). This locality records a negative  $\delta^{13}\text{C}_{\text{OM}}$  excursion of  $-2.8\%$  from

442 pre- to syn-PETM (Fig. 5), in agreement with the CIE excursion of 3-5 ‰ identified in other southern Pyrenean  
443 sections and other global settings (e.g. Schmitz et al., 2001; Schmitz and Pujalte, 2007; McInerney and Wing,  
444 2011; Pujalte et al., 2015). The slightly reduced magnitude compared to the global record is consistent with  
445 observed systematic differences in the CIE across different types of terrestrial archives, with paleosol carbonates  
446 typically recording a 1-2 ‰ larger CIE than paleosol organic matter (Bowen et al., 2004; Cotton et al., 2015;  
447 Gallagher et al., 2019). We do not identify the POE in the Rin section, and we suggest that it may have been  
448 missed due to its occurrence further down in the section. Likewise, the recovery to pre-PETM values is also largely  
449 absent, with just one sample below the Alevolina Limestone showing less depleted  $\delta^{13}\text{C}_{\text{OM}}$  values.  
450

451 The five members recognised in the Claret Fm. show an evolution from the eastern terrestrial setting into the  
452 western marine domain. At Esplugafreda (Fig. 6), the five members are recorded (Basilici et al., 2022 and  
453 references therein), including Member 1, IVF (pre-PETM); Member 2, the Claret Conglomerate (Onset at  
454 Esplugafreda); Member 3, Yellowish soils (syn-PETM, or body of the PETM); Member 4, red paleosols with  
455 gypsum; and Member 5, consisting of red mudstones with carbonate nodules (e.g. Schmitz and Pujalte, 2007;  
456 Baceta et al., 2011; Pujalte et al., 2014; Colomera et al., 2017; Basilici et al., 2022). However, Member 4, the  
457 gypsum-rich member, only occurs in the eastern part of the basin (Pujalte et al., 2014). Given the coastal position  
458 of the Rin section, at the marine-continental transition and only ~20 km east of the Serraduy section, representing  
459 the westernmost expression of the interfingering between continental deposits from the Esplugafreda Fm. and  
460 marine carbonates (Prieur et al., 2025), the absence of Member 4 supports a further downstream position of the  
461 Rin section relative to the Esplugafreda floodplain section.

462  
463 Duller et al. (2019) estimated a lag time of approximately  $16.5 \pm 7.5$  kyr between the CIE and the onset of coarse-  
464 grained deposition at terrestrial sites in the Pyrenees. While sections such as Tendrui, Claret, and Campo (Pujalte  
465 et al., 2009; Domingo et al., 2009) display a stratigraphic offset consistent with this lag, the Esplugafreda section  
466 does not show such an offset (Duller et al., 2019). In the Rin section discussed here, we observe a clear offset  
467 between the onset of the CIE and the arrival of the Claret Conglomerate (Fig. 5). To correctly position the lag  
468 time and explore the missing POE, future work could focus on high-resolution  $\delta^{13}\text{C}$  characterisation of the section.  
469

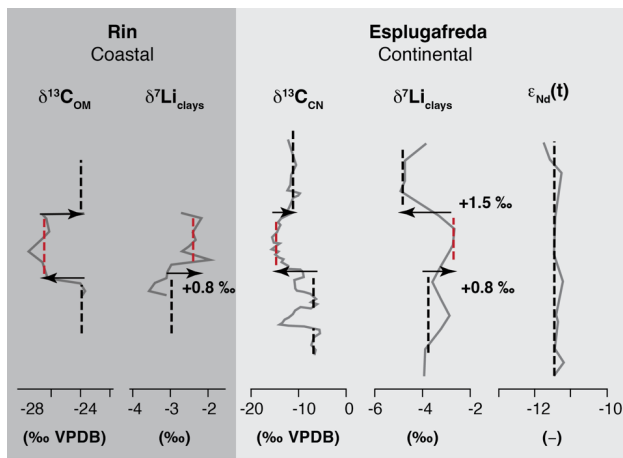
470 The clay mineralogy at Rin further suggests a potential signal propagation effect. A shift from smectite-dominated  
471 clays during the pre-PETM interval to an increase in kaolinite during the syn-PETM interval (Fig. 5D) could  
472 indicate a transition to more hydrolysing conditions and to an increase in weathering intensity, or enhanced erosion  
473 of former sedimentary formations rich in kaolinite. However, this trend also corresponds to a downstream  
474 transition from authigenic smectite-rich paleosols at Esplugafreda (Fig. 6D) (e.g. Khozyem, 2013; Basilici et al.,  
475 2022; Jaimes-Gutierrez et al., 2024) to kaolinite-dominated sediments in the Zumaia deep-marine section  
476 (Gawenda et al., 1999; Schmitz et al., 2001; Bolle and Adatte, 2001). This mineralogical gradient from  
477 Esplugafreda to Rin and Zumaia underscores the system connectivity across the basin (Pujalte et al., 2014).  
478 However, such variations in clay composition may also reflect differences in sediment provenance (although  
479 temporal changes are not observed in the  $\epsilon_{\text{Nd}}$  record from Esplugafreda); differential mineral transport; enhanced  
480 floodplain weathering; an increased proportion of eroded sedimentary formations downstream, bringing reworked  
481 kaolinite (Pujalte et al., 2015); or a larger catchment area feeding the marine system (Chamley, 1989 and  
482 references therein).

483  
484 An influence from Marine Authigenic Aluminosilicate Clay (MAAC) formation is feasible in the coastal setting  
485 of the Rin section, but is unlikely to have been a significant driver of changes in the lithium isotope record given  
486 the dominance of continental inputs. In marine sediments, clay mineral assemblages dominated by kaolinite, illite,  
487 smectite, and mixed-layer illite/smectite are generally interpreted as mainly detrital in origin, reflecting  
488 continental weathering and fluvial transport rather than in situ marine precipitation (Thiry, 2000; Fagel, 2007;  
489 Velde and Meunier, 2008). Although the authigenic formation of these clay minerals is known to occur in marine  
490 environments, it is typically restricted to specific conditions or processes, such as the alteration of volcanic ash,  
491 or evaporitic or hydrothermal settings, and is therefore not expected to be significant in shallow, nearshore  
492 depositional systems with high terrigenous sedimentation rates (Srodon, 2001; Wise et al., 2001; Meunier, 2005).  
493 In contrast to glauconite or other green clays, which may form authigenically under low sedimentation rates,  
494 kaolinite and illite in coastal marine settings are widely regarded as inherited from continental sources (Thiry,  
495 2000; Meunier, 2005; Fagel, 2007; Presti and Michalopoulos, 2008; Bernhardt et al., 2020). Given the dominantly  
496 continental depositional setting of the Rin section and the large detrital clay input inferred for the nearshore  
497 environment, any MAAC contribution is expected to have been minor relative to the terrigenous signal. MAAC  
498 form from isotopically heavy seawater or porewaters and are therefore expected to have  $\delta^7\text{Li}$  values substantially  
499 higher than detrital clays (Pogge von Strandmann et al., 2021a). A simple mass balance indicates that even under  
500 extreme assumptions (e.g. 2 wt.% MAAC, 10‰  $\delta^7\text{Li}$  values), such a contribution would shift bulk values by  
501 <0.3‰, far smaller than the observed PETM excursion.

- Formatted: English (US)
- Formatted: English (US)
- Deleted: coarse-grained sediments, specifically
- Deleted: M
- Deleted: m
- Formatted: Font: 10 pt, Font colour: Text 1
- Formatted: Font: 10 pt, Font colour: Text 1
- Formatted: Font: 10 pt, Font colour: Text 1
- Formatted: Font: 10 pt, Font colour: Text 1
- Formatted: Font: 10 pt, Font colour: Text 1
- Deleted: is possible
- Deleted:
- Formatted: Font: 10 pt, Font colour: Text 1
- Formatted: Font: 10 pt, Font colour: Text 1
- Formatted: Font: 10 pt, Font colour: Text 1
- Formatted: Font: 10 pt, Font colour: Text 1
- Deleted: Firstly, the paleo depositional setting was coastal but dominantly continental. Furthermore,
- Deleted: i
- Formatted: Font: 10 pt, Font colour: Text 1
- Deleted: A
- Deleted: in marine environments
- Deleted: but
- Formatted: Font: 10 pt, Font colour: Text 1
- Formatted: Font: 10 pt, Font colour: Text 1
- Formatted: Font: 10 pt, Font colour: Text 1
- Deleted: -
- Formatted: Font: 10 pt, Font colour: Text 1
- Formatted: Font: 10 pt, Font colour: Text 1
- Deleted: -
- Deleted: aluminosilicate
- Deleted: therefore
- Deleted: (Presti and Michalopoulos, 2008; Bernhardt et al., 2020)...
- Formatted: Font: 10 pt, Font colour: Text 1
- Formatted: Font: Symbol
- Formatted: Superscript
- Formatted: English (US)
- Formatted: Font: Symbol
- Formatted: Superscript
- Formatted: English (US)
- Deleted: ¶
- Formatted: English (US)

## 5.2. Evolution of weathering intensity in the continental realm of the Southern Pyrenees

522 Our  $\delta^7\text{Li}_{\text{clays}}$  records from Rin and Esplugafreda both show a positive ( $\sim 1\text{‰}$ ) lithium isotope excursion in the  
 523 continental Southern Pyrenees during the onset and body of the PETM (Fig. 7). The  $\delta^7\text{Li}$  values from carbonate  
 524 nodules at Rin show greater variability (Fig. 5C), but remain inconclusive due to potential clay contamination or  
 525 cation exchange between clays and carbonates (e.g. Pogge von Strandmann et al., 2019). Given the high Li content  
 526 in silicate minerals, even a minor clay particle content in the nodules could contaminate the carbonate signature.  
 527 Critically, the invariant  $\epsilon_{\text{Nd}}$  composition of both size fractions throughout the Esplugafreda record (Fig. 6C)  
 528 supports a constant provenance of the sediments, which suggests that the  $\delta^7\text{Li}_{\text{clays}}$  records can be reliably  
 529 interpreted as a reflection of weathering regime changes in response to the climatic perturbation.  
 530



533 **Figure 7.** Comparison of isotopic results from the Rin and Esplugafreda sections. Grey solid lines show the raw  
 534 data, while dashed black and red lines indicate typical values for different intervals, where red represents the  
 535 PETM. The pre-PETM and post-PETM shifts are indicated with the black arrows, and the magnitudes of the  
 536  $\delta^7\text{Li}_{\text{clays}}$  excursions are reported.  
 537

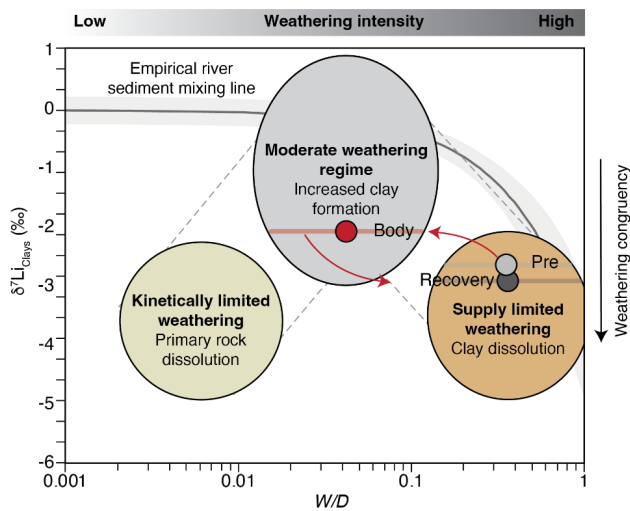
538 In many other PETM records, both marine and terrestrial  $\delta^7\text{Li}$  values show a negative excursion from pre-PETM  
 539 to syn-PETM conditions. Pogge von Strandmann et al. (2021) documented a negative  $\delta^7\text{Li}$  excursion of  $\sim 3\text{‰}$   
 540 during the PETM in several marine carbonate sections and in detrital shales, indicating intensified global erosion  
 541 rates (by 2–3 $\times$ ) and a 50–60% increase in silicate weathering fluxes, which was proposed to have contributed to  
 542 climate stabilisation. Ramos et al. (2022) also found a negative  $\delta^7\text{Li}_{\text{clays}}$  excursion, albeit with a smaller magnitude  
 543 of  $\sim 1.5\text{‰}$ , in fine sediments of the Bighorn Basin, North America during the PETM, and this change was sustained  
 544 during the recovery phase. Consistent with these results, Chen et al. (2023) found a negative  $\delta^7\text{Li}_{\text{clays}}$  excursion of  
 545  $\sim 3\text{‰}$  in the Nanyang Basin, East Asia, which, together with the negative  $\delta^7\text{Li}$  excursion in the lacustrine  
 546 carbonates, was interpreted as recording a doubling of the regional silicate weathering intensity during the PETM.  
 547

548 Why, then, do the Southern Pyrenees floodplains record a positive  $\delta^7\text{Li}_{\text{clays}}$  excursion during the PETM? We  
 549 interpret the positive  $\delta^7\text{Li}_{\text{clays}}$  excursion during the PETM as a shift towards increased incongruent weathering  
 550 (moderate weathering regime), characterised by enhanced clay formation in the floodplain deposits. This regime  
 551 would be characterised by increased chemical weathering, but relatively greater increases in physical erosion and  
 552 sediment transport (e.g. Pujalte et al., 2015; Chen et al., 2018; Prieur et al., 2024), due to enhanced runoff causing  
 553 short water residence times and rapid sediment export (i.e. lower  $W/D$ ; Fig. 8). Hydrological changes during the  
 554 PETM are widely documented in the Southern Pyrenees (Schmitz and Pujalte, 2007; Pujalte et al., 2015; Chen et  
 555 al., 2018; Rush et al., 2021; Prieur et al., 2024, 2025; Jaimes-Gutierrez et al., 2024) and likely played a central  
 556 role in driving those weathering changes. A shift towards more intense, episodic rainfall, without an increase in  
 557 mean annual precipitation (Rush et al., 2021), could have reduced infiltration, increased runoff, and shortened  
 558 water–mineral interaction times. These processes would lead to decreased clay formation in the uplands by

559 shortening water-rock interaction times (Kump et al., 2000; Riebe et al., 2004), while shifting clay production and  
 560 accumulation towards lowland environments, where longer sediment residence times promote authigenic clay  
 561 formation, consistent with modern river floodplain processes (e.g. Dellinger et al., 2015; Maffre et al., 2020). We  
 562 also note that weathering processes are highly heterogeneous, and therefore global variability during the PETM  
 563 can be expected (e.g. Frings, 2019). Critically, A decrease in  $W/D$  can lead both to positive or negative  $\delta^7\text{Li}$   
 564 excursions, depending on the starting weathering regime (Krause et al., 2023).

566 Increasing evaporation, as recorded by gypsum lenses in Esplugafreda (Baceta et al., 2011; Khozyem, 2013;  
 567 Jaimes-Gutierrez et al., 2024 and references therein), could also result in oversaturated pore waters, favouring  
 568 clay formation. Experimental and field-based studies show that enhanced evaporation and reduced water  
 569 availability increase the dissolved  $\delta^7\text{Li}$  values in soil and pore waters, leading to higher  $\delta^7\text{Li}$  compositions of clays  
 570 forming in equilibrium with these fluids (Xu et al., 2022; Pogge von Strandmann et al., 2023). Hydrological  
 571 controls can also influence the  $\delta^7\text{Li}_{\text{clays}}$  signatures by regulating water-rock interactions, sediment transport, and  
 572 secondary mineral formation (Fig. 8). In supply-limited weathering regimes, increased runoff shortens water-  
 573 rock interaction times and lowers dissolved  $\delta^7\text{Li}$  values in river waters (Zhang et al., 2022), while enhanced  
 574 sediment transfer promotes sediment storage and prolonged water-sediment interaction in floodplains, where  
 575 continued clay alteration and isotopic re-equilibration can yield relatively higher  $\delta^7\text{Li}$  values in the clay fraction  
 576 preserved in lowland deposits. Overall, rapid sediment transport limits basin-scale weathering intensity, despite  
 577 localised clay formation in floodplain environments.

578



579 **Figure 8.** Weathering regime change from pre-PETM to syn-PETM based on  $\delta^7\text{Li}_{\text{clays}}$  in the continental deposits  
 580 of the Southern Pyrenees. The floodplain records were characterised by a decrease in weathering intensity and  
 581 an increase in clay formation. Enhanced transport efficiency resulted in a major increase in physical erosion,  
 582 with reaction kinetics limiting chemical weathering. Modified from Dellinger et al. (2015, 2017). At low  $W/D$ , the  
 583 empirical river sediment mixing line includes the effects of mixing with primary minerals.  
 584

585 In the Esplugafreda section, the Recovery phase sees a shift towards more negative values than the pre-PETM  
 586 conditions. During this interval, we observe a coeval increase in illite, kaolinite, and chlorite abundances in the  
 587 Esplugafreda section (Jaimes-Gutierrez et al., 2024). This shift in the clay mineral assemblage strongly suggests  
 588 an increase in detrital input. For this reason, we consider that the observed excursion cannot be straightforwardly  
 589 interpreted as a change in weathering intensity, but rather reflect the clay mineral assemblage (Fig. S2).

590  
 591 Temperature effects on lithium isotope fractionation are minor in the Southern Pyrenees. While lithium isotope  
 592 fractionation during clay formation is temperature-dependent (Vigier et al., 2008; Li and West, 2014), the  
 593 fractionation factor ( $\alpha$ ) for incorporation in smectite is nearly constant across typical surface weathering  
 594 temperatures (Vigier et al., 2008). Using the  $\sim 3^\circ\text{C}$  warming estimated for the continental Pyrenees across the  
 595 PETM (Jaimes-Gutierrez et al., 2024), the maximum temperature-driven change in clay  $\delta^7\text{Li}$  values is expected  
 596 to be only a few tenths of a per mil (Li and West, 2014). This effect would shift clay  $\delta^7\text{Li}$  values slightly towards

Deleted: Jaimes-Gutierrez et al. (2024)

598 heavier values and could therefore contribute marginally to the observed excursion, but it is insufficient to explain  
599 the full magnitude of the  $\sim 1\%$  positive  $\delta^7\text{Li}_{\text{clays}}$  shift observed in the records. Hence, climatic and hydrological  
600 processes, rather than direct temperature effects, must dominate the  $\delta^7\text{Li}$  signal.

601  
602 The differences in  $\delta^7\text{Li}$  values between river water and bedrock are controlled by the balance between lithium  
603 release by mineral dissolution and lithium removal by secondary mineral formation (Bouchez et al., 2013). The  
604 Southern Pyrenees during the PETM was a relatively high-erosion regime, such that physical erosion dominated,  
605 increasing the sediment supply and exposing fresh minerals (Schmitz and Pujalte, 2007; Pujalte et al., 2015, 2016;  
606 Chen et al., 2018; Prieur et al., 2024, 2025). When erosion exposes fresh minerals, weathering rates increase with  
607 total denudation, albeit less strongly than the increases in erosion, consistent with shared controls on chemical  
608 weathering and physical denudation rates (Riebe et al., 2004; West et al., 2005). Even though high-relief regions  
609 produce weakly weathered sediments, their high sediment yields and moderate clay formation rates result in  
610 elevated weathering fluxes (Gaillardet et al., 1999). Therefore, we propose that the Southern Pyrenean floodplains  
611 record a shift from a high-weathering intensity regime to a moderate-weathering intensity regime during the  
612 PETM (Fig. 8). The pre-PETM conditions were characterised by a low reactivity of the parent lithology (Kump  
613 and Arthur, 1997; Caves Rugenstein et al., 2019), associated with the carbonate-rich, reworked sediments in the  
614 floodplain deposits, and hence low total weathering fluxes. The above scenario is also consistent with the "system-  
615 clearing" event documented in western North America (Foreman et al., 2012), where sediment transport surged  
616 in response to rapid climatic forcing, as well as with other Eocene warming events such as the Mid-Eocene  
617 Climatic Optimum, which saw a shift towards enhanced clay formation and a lower weathering intensity (Krause  
618 et al., 2023).

619  
620 The progressive increase in kaolinite content from Esplugafreda to Rin may reflect an evolving weathering signal  
621 during sediment transport from the hinterland towards the coastal plains, which potentially extended into the  
622 marine realm. This scenario supports a basin-wide connectivity between climate-driven terrestrial processes and  
623 marine sedimentary records. In addition, the increase in kaolinite content from Esplugafreda to Rin supports a  
624 shift in clay formation processes during the PETM. Kaolinite is typically associated with intense leaching and  
625 more advanced weathering, often forming under warm, humid, and periodically saturated conditions (Chamley,  
626 1989; Velde and Meunier, 2008). Hence, its enrichment suggests either intensified in-situ clay formation in the  
627 floodplains or increased transport of weathered material from the uplands to the lowlands. In either case, this shift  
628 implies greater clay mineral production, consistent with a more incongruent weathering regime driving the  
629 observed positive  $\delta^7\text{Li}_{\text{clays}}$  excursion. Alternatively, enhanced kaolinite supply from the erosion-driven  
630 exhumation of older sediments cannot be ruled out based on the current evidence.

631  
632 Despite these insights, key questions remain unresolved. In particular, a comprehensive study of the provenance  
633 and evolution of clay mineralogy is still needed to determine to what extent the observed patterns along the  
634 sediment routing system reflect changes in weathering intensity, differential mineral transport, or sediment  
635 reworking. Equally important is the need to constrain the precise age of the clay formation in relation to the timing  
636 of the different phases of the PETM, which is critical for reconstructing the temporal dynamics of the weathering  
637 regime in the Southern Pyrenees. Addressing these gaps will be crucial for better understanding how continental  
638 weathering systems responded to extreme climatic perturbations in the past and how they may behave under future  
639 global warming scenarios.

## 641 6. Conclusions

642 We explored the silicate weathering response to the PETM in two terrestrial sections from the Tremp-Graus Basin  
643 of the Southern Pyrenees. These floodplain records show a positive  $\delta^7\text{Li}_{\text{clays}}$  excursion, contrasting with the  
644 commonly observed global negative  $\delta^7\text{Li}$  excursion in clays and carbonates. We interpret this excursion as  
645 reflecting a shift towards a moderate-intensity, incongruent weathering regime from an initial high-intensity,  
646 supply-limited regime. The high erosion rates associated with increased extreme rainfall events and channel  
647 mobility may have been the central factor influencing sediment residence times, with rapid sediment transport  
648 limiting the extent of chemical weathering. Nevertheless, the elevated denudation rates would have led to higher  
649 sediment and dissolved cation fluxes to the ocean, thereby enhancing regional  $\text{CO}_2$  drawdown.

650  
651 We explored two potential archives for recording continental weathering processes using lithium isotopes. The  
652 clay records show a distinct response, reflected in positive  $\delta^7\text{Li}_{\text{clays}}$  excursions synchronous with the negative CIE.  
653 However, the  $\delta^7\text{Li}_{\text{nodules}}$  signal recorded in the carbonate nodules is less conclusive, and we interpret the high  
654 temporal variability as a sign of potential contamination by clays in the nodules. Given that Li concentrations in  
655 silicate minerals are higher than in carbonates by several orders of magnitude, even minor amounts of clays could

Deleted: ¶

657 have resulted in a mixed response in the nodules. Future studies should explore weaker leaching approaches on  
658 such nodules and seek to validate such data with major and trace element analyses.

659  
660 Provided coeval formation, the increase in kaolinite content from Esplugafreda to Rin provides mineralogical  
661 support for more hydrolysing conditions and clay formation during the PETM in the Tremp-Graus Basin,  
662 reinforcing the interpretation of more incongruent weathering under altered hydroclimatic conditions. Notably,  
663 the parent material in these floodplain paleosols is carbonate-rich and relatively unreactive. These results highlight  
664 the critical role of hydrological controls, especially rainfall intensity, runoff dynamics, and sediment residence  
665 time, in shaping continental weathering responses during extreme climate events.

666  
667 Finally, we propose that to fully quantify weathering dynamics during the PETM in the Southern Pyrenees, further  
668 work is needed to: (1) constrain the chronology of clay formation; (2) trace the evolution of clay mineralogy and  
669 provenance from source to sink; and (3) integrate continental and marine weathering records across the sediment  
670 routing system. Together, these steps will be essential for refining our understanding of weathering behaviour and  
671 the associated climate feedbacks under rapid climatic perturbations, and for improving predictions of Earth's  
672 surface processes in semi-arid floodplain systems in future global warming scenarios.

#### 674 **Acknowledgments**

675 We acknowledge funding from the European Union's Horizon 2020 research and innovation programme under  
676 the Marie Skłodowska-Curie grant agreement No. 860383 S2S FUTURE. D.J.W. was supported by a NERC  
677 independent research fellowship (NE/T011440/1). We thank Justine Blondet for her support in neodymium  
678 isotope chromatography. We thank Dr. Gaojun Li and an anonymous reviewer for their constructive comments  
679 that helped improve the manuscript.

#### 680 **Author contributions**

681 R.J.G. performed sample collection, analytical work (clay mineralogy, RockEval, lithium and neodymium ion-  
682 exchange chromatography), data interpretation, visualisation, and original manuscript writing.  
683 M.P. contributed to sample collection, data interpretation, visualisation, and manuscript writing.  
684 D.J.W. and P.A.E.P.V.S. contributed to analytical work on lithium isotopes, data interpretation, and manuscript  
685 writing.  
686 E.P. conducted analytical work on neodymium isotopes, data interpretation, and manuscript writing.  
687 T.A. conducted RockEval analyses, contributed to data interpretation, and manuscript writing.  
688 J.E.S. conducted  $\delta^{13}\text{C}$  analyses on organic matter and contributed to data interpretation and manuscript writing.  
689 S.C. acquired funding for the project, contributed to sample collection, data interpretation, and manuscript writing.

#### 692 **Conflict of interest**

693 The authors declare that they have no conflict of interest relevant to this study.

#### 694 **References**

- 695  
696 Adatte, T., Stinnesbeck, W., and Keller, G., 1996, Lithostratigraphic and mineralogic correlations of near K/T  
697 boundary clastic sediments in northeastern Mexico: Implications for origin and nature of deposition, *in*  
698 *The Cretaceous-Tertiary Event and Other Catastrophes in Earth History*, Geological Society of  
699 America, doi:10.1130/0-8137-2307-8.211.
- 700 Anderson, S.P., Von Blanckenburg, F., and White, A.F., 2007, Physical and Chemical Controls on the Critical  
701 Zone: *Elements*, v. 3, p. 315–319, doi:10.2113/gselements.3.5.315.
- 702 Baceta, J.I., Pujalte, V., and Bernaola, G., 2005, Paleocene coralgal reefs of the western Pyrenean basin,  
703 northern Spain: New evidence supporting an earliest Paleogene recovery of reefal ecosystems:  
704 *Palaeogeography, Palaeoclimatology, Palaeoecology*, v. 224, p. 117–143,  
705 doi:10.1016/j.palaeo.2005.03.033.
- 706 Baceta, J.I., Pujalte, V., Wright, V.P., and Schmitz, B., 2011, Carbonate platform models, sea/ level changes and  
707 extreme climatic events during the Paleocene/ Eocene greenhouse interval: A basin-platform-coastal  
708 plain transect across the southern Pyrenean basin: 28th IAS Meeting of Sedimentology.

Deleted: , and provided supervision

Formatted: English (US)

Deleted: , and provided supervision

Formatted: English (US)

Deleted: , and provided supervision

- 712 Barefoot, E.A., Nittrouer, J.A., Foreman, B.Z., Hajek, E.A., Dickens, G.R., Baisden, T., and Toms, L., 2022,  
713 Evidence for enhanced fluvial channel mobility and fine sediment export due to precipitation  
714 seasonality during the Paleocene-Eocene thermal maximum: v. 50, p. 116–120, doi:10.1130/G49149.1.
- 715 Basilici, G., Colombera, L., Soares, M.V.T., Arévalo, O.J., Mountney, N.P., Lorenzoni, P., de Souza Filho,  
716 C.R., Mesquita, Á.F., and Janočko, J., 2022, Variations from dry to aquatic conditions in Vertisols  
717 (Esplugafreda Formation, Eastern Pyrenees, Spain): Implications for late Paleocene climate change:  
718 Palaeogeography, Palaeoclimatology, Palaeoecology, v. 595, p. 110972,  
719 doi:10.1016/j.palaeo.2022.110972.
- 720 Bauer, K.K., Vennemann, T.W., and Gilg, H.A., 2016, Stable isotope composition of bentonites from the Swiss  
721 and Bavarian Freshwater Molasse as a proxy for paleoprecipitation: Palaeogeography,  
722 Palaeoclimatology, Palaeoecology, v. 455, p. 53–64, doi:10.1016/j.palaeo.2016.02.002.
- 723 Bayon, G., Burton, K.W., Soulet, G., Vigier, N., Dennielou, B., Etoubleau, J., Ponzevera, E., German, C.R., and  
724 Nesbitt, R.W., 2009, Hf and Nd isotopes in marine sediments: Constraints on global silicate  
725 weathering: Earth and Planetary Science Letters, v. 277, p. 318–326, doi:10.1016/j.epsl.2008.10.028.
- 726 Bayon, G., German, C.R., Boella, R.M., Milton, J.A., Taylor, R.N., and Nesbitt, R.W., 2002, An improved  
727 method for extracting marine sediment fractions and its application to Sr and Nd isotopic analysis:  
728 Chemical Geology, v. 187, p. 179–199, doi:10.1016/S0009-2541(01)00416-8.
- 729 Behar, F., Beaumont, V., and De B. Penteadó, H.L., 2001, Rock-Eval 6 Technology: Performances and  
730 Developments: Oil & Gas Science and Technology, v. 56, p. 111–134, doi:10.2516/ogst.2001013.
- 731 Bernhardt, A., Oelze, M., Bouchez, J., Von Blanckenburg, F., Mohtadi, M., Christl, M., and Wittmann, H.,  
732 2020,  $^{10}\text{Be}/^9\text{Be}$  Ratios Reveal Marine Authigenic Clay Formation: Geophysical Research Letters, v.  
733 47, p. e2019GL086061, doi:10.1029/2019GL086061.
- 734 Bolle, M.-P., and Adatte, T., 2001, Palaeocene- early Eocene climatic evolution in the Tethyan realm: clay  
735 mineral evidence: Clay Minerals, v. 36, p. 249–261, doi:10.1180/000985501750177979.
- 736 Bouchez, J., Von Blanckenburg, F., and Schuessler, J.A., 2013, Modeling novel stable isotope ratios in the  
737 weathering zone: American Journal of Science, v. 313, p. 267–308, doi:10.2475/04.2013.01.
- 738 Bouvier, A., Vervoort, J.D., and Patchett, P.J., 2008, The Lu–Hf and Sm–Nd isotopic composition of CHUR:  
739 Constraints from unequilibrated chondrites and implications for the bulk composition of terrestrial  
740 planets: Earth and Planetary Science Letters, v. 273, p. 48–57, doi:10.1016/j.epsl.2008.06.010.
- 741 Bowen, G.J., Beerling, D.J., Koch, P.L., Zachos, J.C., and Quattlebaum, T., 2004, A humid climate state during  
742 the Palaeocene/Eocene thermal maximum: Nature, v. 432, p. 495–499, doi:10.1038/nature03115.
- 743 Bufer, A., Hovius, N., Emberson, R., Rugenstein, J.K.C., Galy, A., Hassenruck-Gudipati, H.J., and Chang, J.-M.,  
744 2021, Co-variation of silicate, carbonate and sulfide weathering drives CO<sub>2</sub> release with erosion:  
745 Nature Geoscience, v. 14, p. 211–216, doi:10.1038/s41561-021-00714-3.
- 746 Carmichael, M.J. et al., 2017, Hydrological and associated biogeochemical consequences of rapid global  
747 warming during the Paleocene-Eocene Thermal Maximum: Global and Planetary Change, v. 157, p.  
748 114–138, doi:10.1016/j.gloplacha.2017.07.014.
- 749 Caves, J.K., Jost, A.B., Lau, K.V., and Maher, K., 2016, Cenozoic carbon cycle imbalances and a variable  
750 weathering feedback: Earth and Planetary Science Letters, v. 450, p. 152–163,  
751 doi:10.1016/j.epsl.2016.06.035.
- 752 Caves Rugenstein, J.K., Ibarra, D.E., and von Blanckenburg, F., 2019, Neogene cooling driven by land surface  
753 reactivity rather than increased weathering fluxes: Nature, v. 571, p. 99–102, doi:10.1038/s41586-019-  
754 1332-y.
- 755 Chamley, H., 1989, Clay Sedimentology: Berlin, Heidelberg, Springer Berlin Heidelberg, doi:10.1007/978-3-  
756 642-85916-8.

Formatted: German (Switzerland)

- 757 Chen, Z., Ding, Z., Yang, S., Sun, J., Zhu, M., Xiao, Y., Tong, F., and Liang, Y., 2023, Strong Coupling  
758 Between Carbon Cycle, Climate, and Weathering During the Paleocene-Eocene Thermal Maximum:  
759 Geophysical Research Letters, v. 50, p. e2023GL102897, doi:10.1029/2023GL102897.
- 760 Chen, C., Guerit, L., Foreman, B.Z., Hassenruck-Gudipati, H.J., Adatte, T., Honegger, L., Perret, M., Sluijs, A.,  
761 and Castellort, S., 2018, Estimating regional flood discharge during Palaeocene-Eocene global  
762 warming: Scientific Reports, v. 8, p. 13391, doi:10.1038/s41598-018-31076-3.
- 763 Colombera, L., Arévalo, O.J., and Mountney, N.P., 2017, Fluvial-system response to climate change: The  
764 Paleocene-Eocene Tremp Group, Pyrenees, Spain: Global and Planetary Change, v. 157, p. 1–17,  
765 doi:10.1016/j.gloplacha.2017.08.011.
- 766 Cotton, J.M., Sheldon, N.D., Hren, M.T., and Gallagher, T.M., 2015, Positive feedback drives carbon release  
767 from soils to atmosphere during Paleocene/Eocene warming: American Journal of Science, v. 315, p.  
768 337–361, doi:10.2475/04.2015.03.
- 769 Dellinger, M., Bouchez, J., Gaillardet, J., Faure, L., and Moureau, J., 2017, Tracing weathering regimes using  
770 the lithium isotope composition of detrital sediments: Geology, v. 45, p. 411–414,  
771 doi:10.1130/G38671.1.
- 772 Dellinger, M., Gaillardet, J., Bouchez, J., Calmels, D., Louvat, P., Dosseto, A., Gorge, C., Alanoca, L., and  
773 Maurice, L., 2015, Riverine Li isotope fractionation in the Amazon River basin controlled by the  
774 weathering regimes: Geochimica et Cosmochimica Acta, v. 164, p. 71–93,  
775 doi:10.1016/j.gca.2015.04.042.
- 776 Dessert, C., Dupré, B., Gaillardet, J., François, L.M., and Allègre, C.J., 2003, Basalt weathering laws and the  
777 impact of basalt weathering on the global carbon cycle: Chemical Geology, v. 202, p. 257–273,  
778 doi:10.1016/j.chemgeo.2002.10.001.
- 779 Dickens, G.R., O’Neil, J.R., Rea, D.K., and Owen, R.M., 1995, Dissociation of oceanic methane hydrate as a  
780 cause of the carbon isotope excursion at the end of the Paleocene: Paleoceanography, v. 10, p. 965–  
781 971, doi:10.1029/95PA02087.
- 782 Domingo, L., López-Martínez, N., Leng, M.J., and Grimes, S.T., 2009, The Paleocene–Eocene Thermal  
783 Maximum record in the organic matter of the Claret and Tendryu continental sections (South-central  
784 Pyrenees, Lleida, Spain): Earth and Planetary Science Letters, v. 281, p. 226–237,  
785 doi:10.1016/j.epsl.2009.02.025.
- 786 Dreyer, T., 1993, Quantified Fluvial Architecture in Ephemeral Stream Deposits of the Esplugafreda Formation  
787 (Palaeocene), Tremp-Graus Basin, Northern Spain, in Marzo, M. and Puigdefàbregas, C. eds., Alluvial  
788 Sedimentation, Wiley, p. 337–362, doi:10.1002/9781444303995.ch23.
- 789 Duller, R.A., Armitage, J.J., Manners, H.R., Grimes, S., and Jones, T.D., 2019, Delayed sedimentary response  
790 to abrupt climate change at the Paleocene-Eocene boundary, northern Spain: Geology, v. 47, p. 159–  
791 162, doi:10.1130/G45631.1.
- 792 Eichenseer, H., 1988, Facies Geology Of Late Maestrichtian To Early Eocene Coastal And Shallow Marine  
793 Sediments (Tremp-Graus Basin, Northeastern Spain):
- 794 Eichenseer, H., and Luterbacher, H., 1992, The marine paleogene of the tremp region (NE Spain)-depositional  
795 sequences, facies history, biostratigraphy and controlling factors: Facies, v. 27, p. 119–151,  
796 doi:10.1007/BF02536808.
- 797 Espitalie, J., Deroo, G., and Marquis, F., 1985, La pyrolyse Rock-Eval et ses applications. Deuxième partie.:  
798 Revue de l’Institut Français du Pétrole, v. 40, p. 755–784, doi:10.2516/ogst:1985045.
- 799 Fagel, N., 2007, Chapter Four Clay Minerals, Deep Circulation and Climate, in Developments in Marine  
800 Geology, Elsevier, v. 1, p. 139–184, doi:10.1016/S1572-5480(07)01009-3.

Formatted: French (Switzerland)

- 801 Foreman, B.Z., Heller, P.L., and Clementz, M.T., 2012, Fluvial response to abrupt global warming at the  
802 Palaeocene/Eocene boundary: *Nature*, v. 491, p. 92–95, doi:10.1038/nature11513.
- 803 Frings, P.J., 2019, Palaeoweathering: How Do Weathering Rates Vary with Climate? *Elements*, v. 15, p. 259–  
804 265, doi:10.2138/gselements.15.4.259.
- 805 Gaillardet, J., Dupré, B., and Allègre, C.J., 1999, Geochemistry of large river suspended sediments: silicate  
806 weathering or recycling tracer? *Geochimica et Cosmochimica Acta*, v. 63, p. 4037–4051,  
807 doi:10.1016/S0016-7037(99)00307-5.
- 808 Gaitan, C.E., Pucéat, E., Pellenard, P., Blondet, J., Bayon, G., Adatte, T., Israel, C., Robin, C., and Guillocheau,  
809 F., 2023, Late Cretaceous erosion and chemical weathering record in the offshore Cape Basin: Source-  
810 to-sink system from Hf Nd isotopes and clay mineralogy: *Marine Geology*, v. 466, p. 107187,  
811 doi:10.1016/j.margeo.2023.107187.
- 812 Gallagher, T.M., Cacciatori, C.G., and Breecker, D.O., 2019, Interpreting the Difference in Magnitudes of  
813 PETM Carbon Isotope Excursions in Paleosol Carbonate and Organic Matter: Oxidation of Methane in  
814 Soils Versus Elevated Soil Respiration Rates: *Paleoceanography and Paleoclimatology*, v. 34, p. 2113–  
815 2128, doi:10.1029/2019PA003596.
- 816 Gawenda, P., Winkler, W., Schmitz, B., and Adatte, T., 1999, Climate and bioproductivity control on carbonate  
817 turbidite sedimentation (Paleocene to earliest Eocene, Gulf of Biscay, Zumaia, Spain): *Journal of*  
818 *Sedimentary Research*, v. 69, p. 1253–1261, doi:10.2110/jsr.69.1253.
- 819 Gibbs, 1977, Clay Mineral Segregation in the Marine Environment: *SEPM Journal of Sedimentary Research*, v.  
820 Vol. 47, doi:10.1306/212F713A-2B24-11D7-8648000102C1865D.
- 821 Goddéri, Y., Donnadiu, Y., Tombozafy, M., and Dessert, C., 2008, Shield effect on continental weathering:  
822 Implication for climatic evolution of the Earth at the geological timescale: *Geoderma*, v. 145, p. 439–  
823 448, doi:10.1016/j.geoderma.2008.01.020.
- 824 Gómez-Gras, D., Roigé, M., Fondevilla, V., Oms, O., Boya, S., and Remacha, E., 2016, Provenance constraints  
825 on the Tremp Formation paleogeography (southern Pyrenees): Ebro Massif VS Pyrenees sources:  
826 *Cretaceous Research*, v. 57, p. 414–427, doi:10.1016/j.cretres.2015.09.010.
- 827 Gutjahr, M., Frank, M., Stirling, C.H., Klemm, V., Van De Fliedert, T., and Halliday, A.N., 2007, Reliable  
828 extraction of a deepwater trace metal isotope signal from Fe–Mn oxyhydroxide coatings of marine  
829 sediments: *Chemical Geology*, v. 242, p. 351–370, doi:10.1016/j.chemgeo.2007.03.021.
- 830 Hessler, A.M., Zhang, J., Covault, J., and Ambrose, W., 2017, Continental weathering coupled to Paleogene  
831 climate changes in North America: *Geology*, v. 45, p. 911–914, doi:10.1130/G39245.1.
- 832 Hilton, R.G., 2023, Earth’s persistent thermostat: *Science*, v. 379, p. 329–330, doi:10.1126/science.adf3379.
- 833 Jaimes-Gutierrez, R., Adatte, T., Pucéat, E., Vennemann, T., Prieur, M., Wild, A.L., Khozyem, H., Vaucher, R.,  
834 and Castellort, S., 2024, Deciphering Paleocene-Eocene Thermal Maximum Climatic Dynamics:  
835 Insights From Oxygen and Hydrogen Isotopes in Clay Minerals of Paleosols From the Southern  
836 Pyrenees: *Paleoceanography and Paleoclimatology*, v. 39, p. e2024PA004858,  
837 doi:10.1029/2024PA004858.
- 838 Jaimes-Gutierrez, R., Vimperc, L., Wilson, D.J., Blaser, P., Adatte, T., Sahoo, S., and Castellort, S., 2025a,  
839 Lithium isotopes reveal enhanced weathering fluxes in North America during the Paleocene–Eocene  
840 Thermal Maximum: *Geology*, doi:https://doi.org/10.1130/G53708.1.
- 841 Jones, M.T. et al., 2023, Tracing North Atlantic volcanism and seaway connectivity across the Paleocene–  
842 Eocene Thermal Maximum (PETM): *Climate of the Past*, v. 19, p. 1623–1652, doi:10.5194/cp-19-  
843 1623-2023.
- 844 Kennett, J.P., and Stott, L.D., 1991, Abrupt deep-sea warming, paleoceanographic changes and benthic  
845 extinctions at the end of the Palaeocene: *Nature*, v. 353, p. 225–229, doi:10.1038/353225a0.

**Deleted:** Jaimes-Gutierrez, R., Vimperc, L., Wilson, D.J., Blaser, P., Pogge von Strandmann, P.A.E., Adatte, T., Swapan, S., and Castellort, S., 2025b, Lithium isotopes reveal enhanced weathering fluxes in North America during the Paleocene–Eocene Thermal Maximum: , p. Preprint, doi:https://doi.org/10.1130/G53708.1.

- 852 Khozyem, H.M.A., 2013, Sedimentology, geochemistry and mineralogy of the Paleocene Eocene Thermal  
853 Maximum (PETM): Sediment records from Egypt, India and Spain [Doctoral Dissertation]: Université  
854 de Lausanne, 195 p.
- 855 Kısakürek, B., James, R.H., and Harris, N.B.W., 2005, Li and  $\delta^7\text{Li}$  in Himalayan rivers: Proxies for silicate  
856 weathering? *Earth and Planetary Science Letters*, v. 237, p. 387–401, doi:10.1016/j.epsl.2005.07.019.
- 857 Krause, A.J., Sluijs, A., Van Der Ploeg, R., Lenton, T.M., and Pogge Von Strandmann, P.A.E., 2023, Enhanced  
858 clay formation key in sustaining the Middle Eocene Climatic Optimum: *Nature Geoscience*, v. 16, p.  
859 730–738, doi:10.1038/s41561-023-01234-y.
- 860 Kump, L.R., and Arthur, M.A., 1997, Global Chemical Erosion during the Cenozoic: Weatherability Balances  
861 the Budgets, *in* Ruddiman, W.F. ed., *Tectonic Uplift and Climate Change*, Boston, MA, Springer US,  
862 p. 399–426, doi:10.1007/978-1-4615-5935-1\_18.
- 863 Kump, L.R., Brantley, S.L., and Arthur, M.A., 2000, Chemical Weathering, Atmospheric  $\text{CO}_2$ , and Climate:  
864 Annual Review of Earth and Planetary Sciences, v. 28, p. 611–667,  
865 doi:10.1146/annurev.earth.28.1.611.
- 866 Li, G., and West, A.J., 2014, Evolution of Cenozoic seawater lithium isotopes: Coupling of global denudation  
867 regime and shifting seawater sinks: *Earth and Planetary Science Letters*, v. 401, p. 284–293,  
868 doi:10.1016/j.epsl.2014.06.011.
- 869 Liu, C.-Y., Wilson, D.J., Hathorne, E.C., Xu, A., and Pogge Von Strandmann, P.A.E., 2023, The influence of  
870 river-derived particles on estuarine and marine elemental cycles: Evidence from lithium isotopes:  
871 *Geochimica et Cosmochimica Acta*, v. 361, p. 183–199, doi:10.1016/j.gca.2023.08.015.
- 872 Maffre, P., Goddérès, Y., Vigier, N., Moquet, J.-S., and Carretier, S., 2020, Modelling the riverine  $\delta^7\text{Li}$   
873 variability throughout the Amazon Basin: *Chemical Geology*, v. 532, p. 119336,  
874 doi:10.1016/j.chemgeo.2019.119336.
- 875 Maher, K., and Von Blanckenburg, F., 2023, The circular nutrient economy of terrestrial ecosystems and the  
876 consequences for rock weathering: *Frontiers in Environmental Science*, v. 10, p. 1066959,  
877 doi:10.3389/fenvs.2022.1066959.
- 878 Mattauer, M., and Henry, J., 1974, Pyrenees: Special Publications, v. 4, no.1, p. 3–21.
- 879 McInerney, F.A., and Wing, S.L., 2011, The Paleocene-Eocene Thermal Maximum: A Perturbation of Carbon  
880 Cycle, Climate, and Biosphere with Implications for the Future: *Annual Review of Earth and Planetary*  
881 *Sciences*, v. 39, p. 489–516, doi:10.1146/annurev-earth-040610-133431.
- 882 Meunier, A., 2005, *Clays*: Berlin ; New York, Springer, 472 p.
- 883 Misra, S., and Froelich, P.N., 2012, Lithium Isotope History of Cenozoic Seawater: Changes in Silicate  
884 Weathering and Reverse Weathering: *Science*, v. 335, p. 818–823, doi:10.1126/science.1214697.
- 885 Moore, D.M., and Reynolds, R.C., 1992, *Moore, Reynolds 1997\_X-Ray Diffraction.pdf*: New York, Oxford  
886 University Press, 401 p.
- 887 Moulton, K.L., West, J., and Berner, R.A., 2000, Solute flux and mineral mass balance approaches to the  
888 quantification of plant effects on silicate weathering: v. 300, p. 539–570.
- 889 Muñoz, J.A., 1992, Evolution of a continental collision belt: ECORS-Pyrenees crustal balanced cross-section, *in*  
890 McClay, K.R. ed., *Thrust Tectonics*, Dordrecht, Springer Netherlands, p. 235–246, doi:10.1007/978-  
891 94-011-3066-0\_21.
- 892 Murray, J., and Jagoutz, O., 2024, Palaeozoic cooling modulated by ophiolite weathering through organic  
893 carbon preservation: *Nature Geoscience*, v. 17, p. 88–93, doi:10.1038/s41561-023-01342-9.

- 894 Pistiner, J.S., and Henderson, G.M., 2003, Lithium-isotope fractionation during continental weathering  
895 processes: *Earth and Planetary Science Letters*, v. 214, p. 327–339, doi:10.1016/S0012-  
896 821X(03)00348-0.
- 897 Pogge von Strandmann, P.A.E., Cosford, L.R., Liu, C.-Y., Liu, X., Krause, A.J., Wilson, D.J., He, X., McCoy-  
898 West, A.J., Gislason, S.R., and Burton, K.W., 2023, Assessing hydrological controls on the lithium  
899 isotope weathering tracer: *Chemical Geology*, v. 642, p. 121801, doi:10.1016/j.chemgeo.2023.121801.
- 900 Pogge von Strandmann, P.A.E.P.V., Dellinger, M., and West, A.J., 2021a, *Lithium Isotopes: A Tracer of Past  
901 and Present Silicate Weathering*: Cambridge University Press, doi:10.1017/9781108990752.
- 902 Pogge Von Strandmann, P.A.E., Fraser, W.T., Hammond, S.J., Tarbuck, G., Wood, I.G., Oelkers, E.H., and  
903 Murphy, M.J., 2019, Experimental determination of Li isotope behaviour during basalt weathering:  
904 *Chemical Geology*, v. 517, p. 34–43, doi:10.1016/j.chemgeo.2019.04.020.
- 905 Pogge von Strandmann, P.A.E., Jenkyns, H.C., and Woodfine, R.G., 2013, Lithium isotope evidence for  
906 enhanced weathering during Oceanic Anoxic Event 2: *Nature Geoscience*, v. 6, p. 668–672,  
907 doi:10.1038/ngeo1875.
- 908 Pogge von Strandmann, P.A.E., Jones, M.T., West, A.J., Murphy, M.J., Stokke, E.W., Tarbuck, G., Wilson,  
909 D.J., Pearce, C.R., and Schmidt, D.N., 2021b, Lithium isotope evidence for enhanced weathering and  
910 erosion during the Paleocene-Eocene Thermal Maximum: *Science Advances*, v. 7, p. eabh4224,  
911 doi:10.1126/sciadv.abh4224.
- 912 Pogge von Strandmann, P.A.E., Kasemann, S.A., and Wimpenny, J.B., 2020, Lithium and Lithium Isotopes in  
913 Earth's Surface Cycles: v. 16, p. 253–258, doi:10.2138/gselements.16.4.253.
- 914 Porder, S., 2019, How Plants Enhance Weathering and How Weathering is Important to Plants: *Elements*, v. 15,  
915 p. 241–246, doi:10.2138/gselements.15.4.241.
- 916 Presti, M., and Michalopoulos, P., 2008, Estimating the contribution of the authigenic mineral component to the  
917 long-term reactive silica accumulation on the western shelf of the Mississippi River Delta: *Continental  
918 Shelf Research*, v. 28, p. 823–838, doi:10.1016/j.csr.2007.12.015.
- 919 Prieur, M. et al., 2025, Climate Control on Erosion: Evolution of Sediment Flux From Mountainous Catchments  
920 During a Global Warming Event, PETM, Southern Pyrenees, Spain: *Geophysical Research Letters*, v.  
921 52, p. e2024GL112404, doi:10.1029/2024GL112404.
- 922 Prieur, M., Whittaker, A.C., Nuriel, P., Jaimes-Gutierrez, R., Garzanti, E., Roigé, M., Sømme, T.O.,  
923 Schlunegger, F., and Castellort, S., 2024, Fingerprinting enhanced floodplain reworking during the  
924 Paleocene–Eocene Thermal Maximum in the Southern Pyrenees (Spain): Implications for channel  
925 dynamics and carbon burial: *Geology*, v. 52, p. 651–655, doi:10.1130/G52180.1.
- 926 Puigdefbregas, C., and Souquet, P., 1986, Tecto-sedimentary cycles and depositional sequences of the Mesozoic  
927 and Tertiary from the Pyrenees: v. 129, p. 173–203.
- 928 Pujalte, V., Baceta, J.I., and Schmitz, B., 2015, A massive input of coarse-grained siliciclastics in the Pyrenean  
929 Basin during the PETM: the missing ingredient in a coeval abrupt change in hydrological regime:  
930 *Climate of the Past*, v. 11, p. 1653–1672, doi:10.5194/cp-11-1653-2015.
- 931 Pujalte, V., Robador, A., Aitor Payros, and Samsó, J.M., 2016, A siliciclastic braid delta within a lower  
932 Paleogene carbonate platform (Ordessa-Monte Perdido National Park, southern Pyrenees, Spain):  
933 Record of the Paleocene–Eocene Thermal Maximum perturbation: *Palaeogeography,  
934 Palaeoclimatology, Palaeoecology*, v. 459, p. 453–470, doi:10.1016/j.palaeo.2016.07.029.
- 935 Pujalte, V., and Schmitz, B., 2005, Revisión de la estratigrafía del Grupo Tremp («Garumniense», Cuenca de  
936 Tremp-Graus, Pirineos meridionales):

Formatted: Spanish

- 937 Pujalte, V., Schmitz, B., and Baceta, J.I., 2014, Sea-level changes across the Paleocene–Eocene interval in the  
938 Spanish Pyrenees, and their possible relationship with North Atlantic magmatism: *Palaeogeography,*  
939 *Palaeoclimatology, Palaeoecology*, v. 393, p. 45–60, doi:10.1016/j.palaeo.2013.10.016.
- 940 Pujalte, V., Schmitz, B., Baceta, J.I., Orue-Etxebarria, X., Bernaola, G., Dinarès-Turell, J., Payros, A.,  
941 Apellaniz, E., and Caballero, F., 2009, Correlation of the Thanetian-Ilerdian turnover of larger  
942 foraminifera and the Paleocene-Eocene thermal maximum: confirming evidence from the Campo area  
943 (Pyrenees, Spain): *Geologica Acta*, v. 7.
- 944 Ramos, E.J. et al., 2024, Competition or collaboration: Clay formation sets the relationship between silicate  
945 weathering and organic carbon burial in soil: *Earth and Planetary Science Letters*, v. 628, p. 118584,  
946 doi:10.1016/j.epsl.2024.118584.
- 947 Ramos, E.J. et al., 2022, Swift Weathering Response on Floodplains During the Paleocene-Eocene Thermal  
948 Maximum: *Geophysical Research Letters*, v. 49, doi:10.1029/2021GL097436.
- 949 Raymo, M.E., and Ruddiman, W.F., 1992, Tectonic forcing of late Cenozoic climate: *Nature*, v. 359, p. 117–  
950 122, doi:10.1038/359117a0.
- 951 Riebe, C.S., Kirchner, J.W., and Finkel, R.C., 2004, Erosional and climatic effects on long-term chemical  
952 weathering rates in granitic landscapes spanning diverse climate regimes: *Earth and Planetary Science*  
953 *Letters*, v. 224, p. 547–562, doi:10.1016/j.epsl.2004.05.019.
- 954 Roest, W.R., and Srivastava, S.P., 1991, Kinematics of the plate boundaries between Eurasia, Iberia, and Africa  
955 in the North Atlantic from the Late Cretaceous to the present: *Geology*, v. 19, p. 613,  
956 doi:10.1130/0091-7613(1991)019<0613:KOTPB>2.3.CO;2.
- 957 Rosenbaum, G., Lister, G.S., and Duboz, C., 2002, Reconstruction of the tectonic evolution of the western  
958 Mediterranean since the Oligocene: *Journal of the Virtual Explorer*, v. 08,  
959 doi:10.3809/jvirtex.2002.00053.
- 960 Roure, F., Choukroune, P., Berastegui, X., Munoz, J.A., Villien, A., Matheron, P., Bareyt, M., Seguret, M.,  
961 Camara, P., and Deraumont, J., 1989, Ecorep deep seismic data and balanced cross sections: Geometric  
962 constraints on the evolution of the Pyrenees: *Tectonics*, v. 8, p. 41–50, doi:10.1029/TC008i001p00041.
- 963 Rush, W.D., Kiehl, J.T., Shields, C.A., and Zachos, J.C., 2021, Increased frequency of extreme precipitation  
964 events in the North Atlantic during the PETM: Observations and theory: *Palaeogeography,*  
965 *Palaeoclimatology, Palaeoecology*, v. 568, p. 110289, doi:10.1016/j.palaeo.2021.110289.
- 966 Rush, W., Zachos, J., Blackburn, T., and Pogge Von Strandmann, P.A.E., 2025, Continuous Sediment Sourcing  
967 and Changes in Weathering During the PETM in the Salisbury Embayment: *Paleoceanography and*  
968 *Paleoclimatology*, v. 40, p. e2025PA005116, doi:10.1029/2025PA005116.
- 969 Schmitz, B., and Pujalte, V., 2007, Abrupt increase in seasonal extreme precipitation at the Paleocene-Eocene  
970 boundary: *Geology*, v. 35, p. 215, doi:10.1130/G23261A.1.
- 971 Schmitz, B., and Pujalte, V., 2003, Sea-level, humidity, and land-erosion records across the initial Eocene  
972 thermal maximum from a continental-marine transect in northern Spain: *Geology*, v. 31, p. 689,  
973 doi:10.1130/G19527.1.
- 974 Schmitz, B., Pujalte, V., and Nunhez-Betelu, K., 2001, Climate and sea-level perturbations during the Initial  
975 Eocene Thermal Maximum: evidence from siliciclastic units in the Basque Basin (Ermua, Zumaia and  
976 Trabakua Pass), northern Spain: *Palaeogeography, Palaeoclimatology, Palaeoecology* 165, p. 299–320.
- 977 Spangenberg, J.E., 2006, Hydrocarbon Biomarkers in the Topla-Mezica Zinc-Lead Deposits, Northern  
978 Karavanke/Drau Range, Slovenia: Paleoenvironment at the Site of Ore Formation:
- 979 Spangenberg, J.E., and Zufferey, V., 2019, Carbon isotope compositions of whole wine, wine solid residue, and  
980 wine ethanol, determined by EA/IRMS and GC/C/IRMS, can record the vine water status—a

- 981 comparative reappraisal: *Analytical and Bioanalytical Chemistry*, v. 411, p. 2031–2043,  
982 doi:10.1007/s00216-019-01625-4.
- 983 Środoń, J., 2001, Quantitative X-Ray Diffraction Analysis of Clay-Bearing Rocks from Random Preparations:  
984 *Clays and Clay Minerals*, v. 49, p. 514–528, doi:10.1346/CCMN.2001.0490604.
- 985 Tanaka, T. et al., 2000, JNdi-1: a neodymium isotopic reference in consistency with LaJolla neodymium:  
986 *Chemical Geology*, v. 168, p. 279–281, doi:10.1016/S0009-2541(00)00198-4.
- 987 Teixell, A., Labaume, P., and Lagabrielle, Y., 2016, The crustal evolution of the west-central Pyrenees revisited:  
988 Inferences from a new kinematic scenario: *Comptes Rendus. Géoscience*, v. 348, p. 257–267,  
989 doi:10.1016/j.crte.2015.10.010.
- 990 Thiry, M., 2000, Palaeoclimatic interpretation of clay minerals in marine deposits: an outlook from the  
991 continental origin: *Earth-Science Reviews*, v. 49, p. 201–221, doi:10.1016/S0012-8252(99)00054-9.
- 992 Tofelde, S., Bernhardt, A., Guerit, L., and Romans, B.W., 2021, Times Associated With Source-to-Sink  
993 Propagation of Environmental Signals During Landscape Transience: *Frontiers in Earth Science*, v. 9,  
994 p. 628315, doi:10.3389/feart.2021.628315.
- 995 Tremblin, M. et al., 2022, Mercury enrichments of the Pyrenean foreland basins sediments support enhanced  
996 volcanism during the Paleocene-Eocene thermal maximum (PETM): *Global and Planetary Change*, v.  
997 212, p. 103794, doi:10.1016/j.gloplacha.2022.103794.
- 998 Velde, B., and Meunier, A., 2008, *The Origin of Clay Minerals in Soils and Weathered Rocks*: Berlin,  
999 Heidelberg, Springer Berlin Heidelberg, doi:10.1007/978-3-540-75634-7.
- 1000 Vigier, N., Decarreau, A., Millot, R., Carignan, J., Petit, S., and France-Lanord, C., 2008, Quantifying Li  
1001 isotope fractionation during smectite formation and implications for the Li cycle: *Geochimica et*  
1002 *Cosmochimica Acta*, v. 72, p. 780–792, doi:10.1016/j.gca.2007.11.011.
- 1003 Vimpere, L. et al., 2023, Carbon isotope and biostratigraphic evidence for an expanded Paleocene–Eocene  
1004 Thermal Maximum sedimentary record in the deep Gulf of Mexico: *Geology*, doi:10.1130/G50641.1.
- 1005 Walker, J.C.G., Hays, P.B., and Kasting, J.F., 1981, A negative feedback mechanism for the long-term  
1006 stabilization of Earth's surface temperature: *Journal of Geophysical Research: Oceans*, v. 86, p. 9776–  
1007 9782, doi:10.1029/JC086iC10p09776.
- 1008 Wei, G.-Y., Pohl, A., Jiang, S., Zhang, H., Wang, W., A. E. Pogge Von Strandmann, P., Maffre, P., Xiong, G.,  
1009 Shen, S., and Zhang, F., 2025, Changes in continental weathering regimes inhibited global marine  
1010 deoxygenation during the Paleocene-Eocene thermal maximum: *Nature Communications*, v. 16, p.  
1011 9163, doi:10.1038/s41467-025-64217-0.
- 1012 Weis, D., Kieffer, B., Maerschalk, C., Pretorius, W., and Barling, J., 2005, High-precision Pb-Sr-Nd-Hf isotopic  
1013 characterization of USGS BHVO-1 and BHVO-2 reference materials: *Geochemistry, Geophysics,*  
1014 *Geosystems*, v. 6, p. 2004GC000852, doi:10.1029/2004GC000852.
- 1015 West, A., Galy, A., and Bickle, M., 2005, Tectonic and climatic controls on silicate weathering: *Earth and*  
1016 *Planetary Science Letters*, v. 235, p. 211–228, doi:10.1016/j.epsl.2005.03.020.
- 1017 Westerhold, T., Röhl, U., McCarren, H.K., and Zachos, J.C., 2009, Latest on the absolute age of the Paleocene–  
1018 Eocene Thermal Maximum (PETM): New insights from exact stratigraphic position of key ash layers  
1019 +19 and –17: *Earth and Planetary Science Letters*, v. 287, p. 412–419, doi:10.1016/j.epsl.2009.08.027.
- 1020 Wilson, D.J., Pogge von Strandmann, P.A.E., White, J., Tarbuck, G., Marca, A.D., Atkinson, T.C., and Hopley,  
1021 P.J., 2021, Seasonal variability in silicate weathering signatures recorded by Li isotopes in cave drip-  
1022 waters: *Geochimica et Cosmochimica Acta*, v. 312, p. 194–216, doi:10.1016/j.gca.2021.07.006.

- 1023 Winnick, M.J., Druhan, J.L., and Maher, K., 2022, Weathering intensity and lithium isotopes: A reactive  
1024 transport perspective: *American Journal of Science*, v. 322, p. 647–682, doi:10.2475/05.2022.01.
- 1025 Wise, S.W., Smellie, J., Aghib, F., Jarrard, R., and Krissek, L., 2001, Authigenic Smectite Clay Coats in CRP-3  
1026 Drillcore, Victoria Land Basin, Antarctica, as a Possible Indicator of Fluid Flow: A Progress Report ,  
1027 p. 281–298.
- 1028 Xu, Z., Li, T., Li, G., Hedding, D.W., Wang, Y., Gou, L.-F., Zhao, L., and Chen, J., 2022, Lithium isotopic  
1029 composition of soil pore water: Responses to evapotranspiration: *Geology*, v. 50, p. 194–198,  
1030 doi:10.1130/G49366.1.
- 1031 Zachos, J.C., Dickens, G.R., and Zeebe, R.E., 2008, An early Cenozoic perspective on greenhouse warming and  
1032 carbon-cycle dynamics: *Nature*, v. 451, p. 279–283, doi:10.1038/nature06588.
- 1033 Zachos, J.C., Wara, M.W., Bohaty, S., Delaney, M.L., Petrizzo, M.R., Brill, A., Bralower, T.J., and Premoli-  
1034 Silva, I., 2003, A Transient Rise in Tropical Sea Surface Temperature During the Paleocene-Eocene  
1035 Thermal Maximum: *Science*, v. 302, p. 1551–1554, doi:10.1126/science.1090110.
- 1036 Zeebe, R.E., Ridgwell, A., and Zachos, J.C., 2016, Anthropogenic carbon release rate unprecedented during the  
1037 past 66 million years: *Nature Geoscience*, v. 9, p. 325–329, doi:10.1038/ngeo2681.
- 1038 Zhang, F., Dellinger, M., Hilton, R.G., Yu, J., Allen, M.B., Densmore, A.L., Sun, H., and Jin, Z., 2022,  
1039 Hydrological control of river and seawater lithium isotopes: *Nature Communications*, v. 13, p. 3359,  
1040 doi:10.1038/s41467-022-31076-y.
- 1041